Adipose Triglyceride Lipase protects the endocytosis of renal cells on a high fat diet in *Drosophila*

Aleksandra Lubojemska[1], M. Irina Stefana[1,2], Lena Lampe[1], Azumi Yoshimura[3], Alana Burrell[3], Lucy Collinson[3] and Alex P. Gould[1*]

[1]Physiology and Metabolism Laboratory, The Francis Crick Institute, Midland Road, London, NW1 1AT, UK

[2]Current address: Wellcome Centre for Human Genetics, University of Oxford, OX3 7BN, UK

[3]Electron Microscopy Science Technology Platform, The Francis Crick Institute, Midland Road, London, NW1 1AT, UK

*Correspondence to: Alex.Gould@crick.ac.uk

Abstract

Obesity-related renal lipotoxicity and chronic kidney disease (CKD) are prevalent pathologies with complex aetiologies. One hallmark of renal lipotoxicity is the ectopic accumulation of lipid droplets in kidney podocytes and in proximal tubule cells. Renal lipid droplets are observed in human CKD patients and in high-fat diet rodent models but their precise role remains unclear. Here, we establish a high-fat diet model in *Drosophila* that recapitulates renal lipid droplets and several other aspects of mammalian CKD. Cell-type specific genetic manipulations show that lipid can overflow from adipose tissue and is taken up by renal cells called nephrocytes. A high-fat diet drives nephrocyte lipid uptake via the multiligand receptor Cubilin, leading to the ectopic accumulation of lipid droplets. These nephrocyte lipid droplets correlate with ER and mitochondrial deficits, as well as with impaired macromolecular endocytosis, a key conserved function of renal cells. Nephrocyte knockdown of diglyceride acyltransferase 1 (DGAT1), overexpression of adipose triglyceride lipase (ATGL) and epistasis tests together reveal that fatty acid flux through the lipid droplet triglyceride compartment protects the ER, mitochondria and endocytosis of renal cells. Strikingly, boosting nephrocyte expression of the lipid droplet resident enzyme ATGL is sufficient to rescue high-fat diet induced defects in renal endocytosis. Moreover, endocytic rescue requires a conserved mitochondrial regulator, peroxisome proliferator-activated receptor-gamma coactivator 1α (PGC1α). This study demonstrates that lipid droplet lipolysis counteracts the harmful effects of a high-fat diet via a mitochondrial pathway that protects renal endocytosis. It also provides a genetic strategy for determining whether lipid droplets in different biological contexts function primarily to release beneficial or to sequester toxic lipids.

Introduction

In diabetic patients, hyperglycemia triggers complex hemodynamic, metabolic and inflammatory changes that can lead to a constellation of renal dysfunctions termed diabetic nephropathy [1,2]. Obesity is a major risk factor for type 2 diabetes and it is thought that once adipose tissue has expanded to its maximum storage capacity, excess lipids then overflow into the bloodstream and trigger lipotoxicity in the kidney and in other peripheral tissues [3-6]. Several mechanisms are thought to contribute to renal lipotoxicity and chronic kidney disease (CKD). For example, the adipo-renal axis is deregulated such that an altered blend of adipokines and other adipose-derived factors produces renal inflammation, fibrosis and oxidative stress, leading to defective glomerular filtration and proteinuria [7,8]. Adipose-derived factors as well as ectopic lipid accumulation in the kidney are thought to impact multiple podocyte, endothelial and proximal tubule functions, at least in part via the promotion of renal insulin resistance [9]. Rodent studies using a high fat diet (HFD) have provided valuable insights into the links between lipotoxicity and CKD. In mice, HFD is sufficient to trigger features of stress and damage in mouse proximal tubule cells, including the endoplasmic reticulum unfolded protein response, lipid peroxidation, and defective albumin reabsorption [10-13]. In both human patients and mouse models, mitochondrial loss and dysfunction are central to the development and progression of CKD [14]. The underlying abnormalities include decreased mitochondrial biogenesis, loss of mitochondrial membrane potential, decreased ATP generation and altered levels of reactive oxygen species (ROS).

One hallmark of CKD lipotoxicity is the accumulation of lipid droplets in podocytes and in proximal tubule epithelial cells. Lipid droplets are intracellular organelles comprising a core of neutral lipids, such as triglycerides, surrounded by a polar lipid monolayer containing many different proteins, some of which function in lipid metabolism [15,16]. Nascent lipid droplets form via a complex process involving neutral lipid synthesis by endoplasmic reticulum (ER) enzymes such as diglyceride acyltransferase 1 (DGAT1) [17,18]. The neutral lipids stored in lipid droplets can then be broken down by lipolysis, mediated via lipid droplet-associated enzymes such as adipose triglyceride lipase (ATGL) [19]. This catabolic process is distinct from lipophagy, which involves lysosomal acid lipase acting upon lipids delivered to autolysosomes via autophagy [20]. As early as the 1930s, lipid droplets were observed as a sign of pathology in podocytes and in proximal tubule cells during renal disease [21,22], yet it has remained unclear whether they play a protective or a harmful role. Resolution of this question is important for understanding CKD mechanisms and will likely require *in vivo* studies of HFD

animal models with cell-type specific manipulations of enzymes that directly regulate the neutral lipid cargo of droplets rather than acting on other aspects of fatty acid metabolism. ATGL is of particular interest here as its specific function in renal cells in HFD and other CKD mouse models is not yet clear, although whole-body knockouts fed a standard diet are known to display proximal tubule damage and podocyte apoptosis [23,24].

The animal model *Drosophila* has powerful genetics for studying the molecular pathogenesis of some human diseases. This approach is possible because of extensive physiological similarities between major fly and human organs, including the kidney [25]. In *Drosophila*, the renal system comprises two anatomically distinct components - Malpighian tubules and nephrocytes [26-28] (**Fig 1A**). Malpighian tubules are excretory cells that also function in salt and water balance, similar to mammalian renal tubules [29,30]. Nephrocytes are podocyte-like cells that regulate the composition of the hemolymph (blood) via a filtration barrier consisting of Sns and Kirre, orthologs of the mammalian slit diaphragm proteins Nephrin and Neph1 [31,32]. Nephrocytes also function like mammalian proximal tubule cells, efficiently reabsorbing macromolecules via a Cubilin-dependent endocytic receptor complex [33,34]. *Drosophila* has thus been used to model several monogenic kidney diseases including steroid-resistant nephrotic syndrome and renal Fanconi syndrome [34,35]. Previous work using *Drosophila* has also shown that chronic high dietary sugar during adulthood increases O-GlycNAcylation, in turn leading to decreased Sns expression and compromised nephrocyte function [36]. Here we establish a *Drosophila* HFD model that recapitulates in nephrocytes the ectopic lipid droplets and cellular dysfunction observed in CKD. This CKD model is then interrogated with cell-type specific genetics and assays for mitochondria and endocytic function to pinpoint the role of lipid droplets in renal lipotoxicity. Genetic rescues and other approaches are then used to test whether lipid droplet enzymes are necessary and sufficient to ameliorate multiple aspects of renal dysfunction induced by HFD exposure.

Results

HFD induces lipid droplets and abnormal nephrocyte ER and mitochondria

We established a *Drosophila* model for diet-induced renal lipotoxicity by raising animals on a high fat diet (HFD) throughout larval development (0-90 h after hatching, see Methods) (**Fig 1B**). Compared to standard diet (STD), HFD did not significantly alter body growth or developmental timing but it did lead to a small increase in the size of nephrocytes (**S1A-S1C Fig**). To begin characterising the effects of HFD on nephrocytes, a neutral lipid dye (LipidTOX) was used to reveal that lipid droplets in pericardial nephrocytes are sparse in STD animals but strikingly abundant in HFD animals (**Fig 1C**). GFP fused to lipid droplet associated hydrolase (LDAH) localizes to the endoplasmic reticulum (ER) and to the surface of lipid droplets [37]. In STD animals, *Dot-GAL4* driven expression of LDAH (*Dot>LDAH::GFP*) specifically in nephrocytes was mostly ER-associated but, in HFD larvae, it predominantly localized to the surface of 1-2 µm diameter lipid droplets that stain strongly with the neutral lipid dye (**Fig 1D**). Hence, chronic exposure to HFD leads to the strong accumulation of nephrocyte lipid droplets. We also observed that HFD markedly decreased the overall volume of ER and mitochondria in nephrocytes, approximately halving the proportion of the total cell volume that each organelle occupies (**Fig 1E**). These observations together show that HFD in *Drosophila*, as in mammals, induces renal lipid droplets and also a deficit in ER and mitochondrial volumes.

Fig 1: High fat diet (HFD) induces lipid droplets and decreases ER and mitochondria in nephrocytes.
(**A**) Diagram comparing the mammalian nephron and the *Drosophila* renal system. *Drosophila* nephrocytes share functions with mammalian kidney podocytes and proximal tubules. *Drosophila* Malpighian tubules are functionally analogous to renal tubules.
(**B**) For the chronic dietary model, larvae are fed either a standard diet (STD) or a high fat diet (HFD) throughout development. The chronic genetic model for lipid overflow on STD utilises a fat-body specific GAL4 driver (*Lpp-GAL4*) to compare fat body overexpression of ATGL (*Lpp>ATGL*) with the control genotype (*Lpp>ctrl*).
(**C**) Lipid droplets (LDs), stained with a neutral lipid dye (LipidTOX), are more abundant in pericardial nephrocytes (dashed outlines) of HFD than STD larvae. Graph quantifies % of nephrocyte volume occupied by lipid droplets in STD and HFD larvae. In this and subsequent graphs, the boxplot encompasses the first to third quartile and shows the median, and whiskers extend from the hinge by 1.5x inter-quartile range. Data points are coloured according to which independent experiment they are from. Data were statistically analysed using linear mixed models (LMMs) followed by a Wald Chi-Squared test. Asterisks show statistical significance (* $p<0.05$, ** $p<0.005$, ***$p<0.0005$) and ns indicates $p>0.05$ in this and all subsequent graphs. See **Table S1** for details of p values and the type of LMM used for all graphs in this study. Scale bar = 50 µm.
(**D**) In pericardial nephrocytes (dashed outlines), LDAH::GFP localizes primarily to the ER (marked with anti-KDEL antibody) in STD larvae but to the surface of ER-associated lipid

droplets (marked with the neutral lipid dye LipidTOX) in HFD larvae. Note that LDAH::GFP induces clustering of lipid droplets [37].
(**E**) Low and high magnification views of pericardial nephrocytes (dotted outlines) from STD and HFD larvae, showing that HFD decreases mitochondria (marked with anti-ATP5A) and endoplasmic reticulum (ER, marked with anti-KDEL) but increases lipid droplets (marked with LipidTOX). Quantitations of ER and mitochondrial volumes are shown as a % of nephrocyte volume in STD and HFD larvae.

HFD compromises nephrocyte endocytosis

An important function of nephrocytes is to resorb circulating proteins and other macromolecules from the hemolymph via Cubilin and Amnionless dependent endocytosis [31,33]. This nephrocyte endocytic function can be quantified by monitoring *ex vivo* uptake of the polysaccharide dextran [31]. A combination of fluorescently labelled 10 kDa and 500 kDa dextrans has previously been used to assess size-selective filtration as well as overall endocytosis [31]. Using this approach, we measured mean dextran intensities in nephrocytes but observed only a modest increase in the 500:10 kDa dextran intensity ratio over an *ex vivo* incubation timecourse of 3 to 20 min (**S2 Fig**). A 30 min *ex vivo* incubation time was therefore subsequently used as a robust readout for nephrocyte endocytosis rather than size-selective filtration. This assay revealed that endocytic uptake of dextran is decreased in the nephrocytes of HFD animals and, although there is cell-to-cell variability, the mean overall reduction is ~50% compared with STD animals (**Fig 2A and 2B**). This finding is further strengthened by a modified *ex vivo* nephrocyte uptake assay that utilised labelled albumin. As with dextran, nephrocyte accumulation of albumin was significantly decreased by HFD (**Fig 2C and 2D**). We therefore conclude that HFD compromises the key renal function of nephrocyte endocytosis.

Fig 2: HFD decreases nephrocyte uptake of dextran and albumin.
(**A-B**) Dextran uptake assay. (A) Nephrocytes from STD and HFD larvae shown after *ex vivo* incubation with labelled 10 kDa (magenta) and 500 kDa (green) dextran. Bottom row shows same field of view with lipid droplets revealed with a neutral lipid stain stain (LipidTOX). Dashed outlines indicate the positions of all nephrocytes in the bottom row but only those that show weak dextran uptake in the top row. (B) Graph shows that uptake of both 10 kDa (magenta) and 500 kDa (green) dextran is significantly higher on STD than on HFD ($p<0.0005$). Scale bar = 30 µm.
(**C-D**) Albumin uptake assay. (C) Nephrocytes from STD and HFD larvae shown after *ex vivo* incubation with labelled bovine serum albumin (FITC-BSA). Bottom row shows same field of view with lipid droplets revealed with a neutral lipid stain (LipidTOX). Dashed outlines indicate the positions of all nephrocytes in the bottom row but only those that show weak albumin uptake in the top row. (D) Graph shows that uptake of albumin is significantly higher on STD than HFD ($p<0.0005$). Scale bar = 50 µm.

To determine the ultrastructural changes associated with HFD compromised endocytosis, we used correlative light electron microscopy (CLEM) with Airyscan confocal microscopy and serial blockface scanning electron microscopy (SBF SEM). The plasma membrane of nephrocytes is organised into a dense undulating network of slit diaphragms and lacunae [31,32,38]. These ultrastructural features of the plasma membrane network are visible with serial blockface scanning electron microscopy (SBF SEM) in both STD and HFD nephrocytes (**Fig 3A**). CLEM analysis of nephrocytes carrying the endogenous *Rab7* gene tagged with *YFP^{myc}*, *Rab7::YFP^{myc}* [*YRab7*, 39], distinguished five endolysosomal compartments according to the "white", "light" or "dark" SEM luminal density, and the Dextran and Rab7 labelling status (**Fig 3A and S3 Fig**). Comparing our CLEM analysis with previous nephrocyte studies [40-42], strongly suggested that the "white" compartment corresponds to a mix of Dextran^{+}Rab7^{-} early endosomes and Dextran^{+}Rab7^{+} endosomes (alpha-vacuoles). The "light" compartment encompasses Dextran^{+}Rab7^{+} endosomes and Dextran^{-}Rab7^{+} late endosomes (beta-vacuoles), whereas the "dark" compartment included both Dextran^{-}Rab7^{+} late endosomes and Dextran^{-}Rab7^{-} lysosomes. Based on this CLEM classification, the "white" and "light" compartments were segmented from the SBF SEM stacks of entire nephrocyte cells to provide the size distributions of endosomes. This segmentation approach revealed that HFD nephrocytes have substantially fewer endosomes than STD nephrocytes (**Fig 3B**). This HFD deficit is particularly striking for endosomes of less than 1µm in diameter and it is likely to account for the observed decrease in the capacity of nephrocytes to uptake macromolecules such as dextran.

Fig 3. HFD decreases the number of nephrocyte endosomes.

(**A**) CLEM images of midsections of STD and HFD nephrocytes expressing Rab7::YFP^{myc} and labelled with Alexa Fluor 568 10kDa dextran. Scale bars are 5µm.
(**B**) Distribution of endosome number versus diameter for one STD and one HFD nephrocyte segmented by SBF SEM according to the "white" and "light" classifications in S3A Fig.

We have provided evidence demonstrating that HFD induces a syndrome of nephrocyte abnormalities including induction of lipid droplets and deficits in the endoplasmic reticulum, mitochondria and endocytic compartment. Many of these abnormalities are strikingly similar to those observed in the proximal tubule cells of HFD mice and CKD patients. This establishes the *Drosophila* HFD paradigm as a useful model for kidney disease. We next combined our new animal model with cell-type specific genetic manipulations in order to identify the mechanisms linking high dietary lipid to nephrocyte dysfunction. In particular, we focused on the role of lipid droplets, determining whether they are beneficial or harmful for renal function.

Renal lipid droplets can be induced via adipose tissue lipolysis and blocked via Cubilin-dependent endocytosis

To define the physiological pathway leading from dietary high fat to nephrocyte lipid droplets, we directly tested the role of lipid overflow from the larval *Drosophila* adipose tissue (fat body) to peripheral tissues [43]. *Lpp-GAL4* was used to drive chronic expression of the adipocyte triglyceride lipase (ATGL) orthologue Brummer [44] in the fat body (*Lpp>ATGL*) (**Fig 1B**). As with HFD, fat-body specific ATGL expression in STD animals did not substantially alter growth, developmental timing or nephrocyte size (**S1D-S1F Fig**). Nevertheless, this genetic manipulation was sufficient to induce robust lipid droplet accumulation in nephrocytes of STD animals, suggesting that lipid overflow from adipose tissue may also be relevant for HFD-induced renal lipid droplets (**Fig 4A and 4B**). Lipid overflow from adipose tissue, like HFD, also lead to a functional deficit in nephrocyte endocytosis, as *Lpp>ATGL* animals also showed impaired dextran uptake (**Fig 4C and 4D**).

In mammalian proximal tubule cells, the Cubilin (Cubn) receptor is known to be involved in the endocytic uptake of lipoproteins as well as proteins [45]. *Dot-GAL4* was therefore used to drive RNA interference (RNAi) for *Drosophila* Cubn specifically in nephrocytes (*Dot>Cubn[i]*). This revealed that, on HFD, *Cubn* is required for the accumulation of nephrocyte lipid droplets (**Fig 4E and 4F**). With the preceding results, this provides evidence supporting the conclusion that HFD leads to excess fat circulating in the hemolymph (blood), which is then endocytosed by nephrocytes via the Cubn receptor and targeted to lipid droplets. Given that Cubn knockdown did not significantly decrease nephrocyte uptake of a labelled free fatty acid (BODIPY FL C12), it is likely that lipoproteins are the major form of circulating fat that contributes to nephrocyte lipid droplets (**Fig 4G and 4H**).

Fig 4: Fat body lipolysis induces and Cubilin-dependent endocytosis blocks renal lipid droplets.

(**A-B**) Confocal panels (A) and quantifications (B) show that lipid droplets (marked with LipidTOX) accumulate in nephrocytes (dashed outlines in A) of STD larvae expressing ATGL in the fat body (*Lpp>ATGL*) but not in controls (*Lpp>*).
(**C-D**) Confocal micrographs (C) and quantifications of dextran mean fluorescence intensity (D) show that *ex vivo* dextran uptake is decreased in nephrocytes of larvae expressing ATGL in the fat body (*Lpp>ATGL*) but not in those of control larvae (*Lpp>*). Similar results are obtained with 10kDa and 500kDa dextrans.
(**E-F**) Confocal micrographs (E) and quantifications (F) show that lipid droplets (marked with LipidTOX) are far less abundant in the nephrocytes (dashed outlines in E) of nephrocyte-specific Cubilin knockdown (*Dot>Cubn[i]*) compared to control (*Dot>)* HFD larvae.
(**G-H**) Confocal micrographs (G) and quantifications of fluorescence intensity (H) show that Cubilin knockdown in nephrocytes (*Dot>Cubn[i]*) does not decrease *ex vivo* uptake of a

fluorescent analogue of a C18 saturated free fatty acid (BODIPY FL C12) by nephrocytes from STD or HFD larvae. Panel G shows BODIPY FL C12 (green) and LipidTOX (magenta).

Boosting ATGL expression rescues HFD-induced nephrocyte dysfunction

Our results show that excess circulating lipids are endocytosed by nephrocytes and targeted to lipid droplets. This raises an important question - what, if any, contribution do lipid droplets make towards HFD-induced renal dysfunction? To identify unambiguous functions for lipid droplets, rather than for fatty acid metabolism more generally, we targeted two enzymes with direct substrates/products corresponding to the triglyceride cargo of droplets, DGAT1/Midway and ATGL/Brummer. Importantly, nephrocyte lipid droplets in HFD animals were efficiently inhibited either by knocking down DGAT1 (*Dot>DGAT1[i]*) or by increasing the expression of ATGL (*Dot>ATGL*) (**Fig 5A**). Systematically comparing the HFD phenotypes of these two genetic manipulations allows the roles of lipid droplet triglycerides to be parsed into synthesis versus lipolysis functions. This comparative strategy revealed that DGAT1 knockdown in HFD nephrocytes gave a small decrease in mitochondrial volume, although it did not significantly decrease ER volume (**Fig 5B and 5C**). Blocking lipid droplets via ATGL expression, however, did significantly increase both mitochondrial and ER volumes in HFD nephrocytes, consistent with partial restoration of these cell parameters towards STD values (**Fig 5B and 5C,** compare with **Fig 1E**). Using the ratiometric dye BODIPY 581/591 C11 to detect lipid peroxidation, we observed no difference between STD and HFD nephrocytes (**S4 Fig**). Furthermore, lipid peroxidation on HFD did not significantly change with ATGL expression but it was strongly elevated with DGAT1 knockdown (**S4 Fig**). Together, these results demonstrate that abrogation of lipid droplets in HFD nephrocytes by increasing ATGL lipolysis is able to rescue significantly the mitochondrial and ER volumes without increasing lipid peroxidation. In contrast, blocking lipid droplet biogenesis in HFD nephrocytes via inactivation of DGAT1 triglyceride synthesis fails to rescue mitochondria and ER and also increases potentially cytotoxic lipid peroxidation.

We next assessed nephrocyte endocytic function. SBF SEM was used to analyse the entire cell volumes of STD, HFD, HFD DGAT1[i], and HFD ATGL nephrocytes (**S1 Movie to S4 Movie**). Using our CLEM classification to segment these four nephrocyte volumes revealed that the HFD-associated decrease in the total number and volume of endosomes is fully rescued by ATGL but not by DGAT1[i] (**Fig 5D and 5E**). In line with this, both the dextran and albumin uptake of HFD nephrocytes were completely rescued by ATGL expression but not by DGAT1 knockdown (**Fig 5F and 5G**). Importantly, DGAT1 knockdown was epistatic to ATGL

expression with respect to nephrocyte dextran uptake (**Fig 5H**). Hence, ATGL protects renal endocytic function via a mechanism requiring triglyceride substrates, rather than by any moonlighting activity of the enzyme. Together, these striking findings show that nephrocyte-specific ATGL expression is sufficient to ameliorate HFD-induced mitochondrial defects and to stimulate full rescue of endocytic function.

Fig 5: ATGL rescues mitochondria and macromolecule uptake of HFD nephrocytes
(**A**) Confocal micrographs of nephrocytes (dotted outlines), stained with a dye for neutral lipids (LipidTOX), and corresponding quantifications showing that LD accumulation observed on HFD in control larvae (Dot>) is almost completely blocked in nephrocyte-specific DGAT1 RNAi (*Dot>DGAT1[i]*) or ATGL expression (*Dot>ATGL*) larvae. Scale bar = 50 µm.
(**B-C**) Quantifications of nephrocyte ER volume (B) and mitochondrial volume (C) for HFD larvae of the control (*Dot>ctrl)*, *Dot>DGAT1[i]* and *Dot>ATGL* genotypes.
(**D-E**) SBF SEM quantifications of total endosome numbers (D) and volumes (E) in STD control (*Dot>ctrl)*, HFD control (*Dot>ctrl)*, HFD *Dot>DGAT1[i]* and HFD *Dot>ATGL* nephrocytes.
(**F-G**) Quantifications of 10kDa and 500kDa dextran uptake (F) and albumin (FITC-BSA) uptake (G) in HFD nephrocytes showing that nephrocyte-specific ATGL expression (*Dot>ATGL*), but not DGAT1 knockdown (*Dot>DGAT1[i]*), rescues HFD nephrocyte endocytic function.
(**H**) Quantifications of nephrocyte uptake of 10kDa and 500kDa dextrans showing that the genetic rescue of HFD nephrocyte endocytic function obtained with nephrocyte-specific ATGL overexpression (*Dot>ATGL*) is blocked by concomitant DGAT1 knockdown (*Dot>DGAT1[i]*).

ATGL rescue of HFD nephrocyte function requires Srl and Delg

We reasoned that *UAS-ATGL* rescue of nephrocyte dysfunction may reflect restoration of HFD-induced downregulation of the endogenous *bmm/ATGL* gene. To test this possibility, a *bmm-GFP* transcriptional reporter (*ATGL-GFP*) was used to monitor *ATGL* gene expression [46]. This approach revealed that HFD leads to a significant decrease in *ATGL* expression (**Fig 6A and 6B**). Together with the ATGL rescue experiments, this suggests that transcriptional downregulation of ATGL could contribute to nephrocyte dysfunction on HFD. Interestingly, *ATGL-GFP* expression in HFD nephrocytes was restored to approximately STD levels by providing exogenous ATGL enzyme (*Dot>ATGL*), suggesting the existence of positive feedback between ATGL activity and *ATGL* transcription (**Fig 6C**). Thus, ATGL in nephrocytes regulates mitochondria as well as the transcription of its own gene, raising the question of whether these two ATGL functions are separate or linked. To address this, we manipulated peroxisome proliferator-activated receptor-gamma coactivator 1α (PGC1α), a transcriptional coactivator that controls mitochondrial biogenesis and energy metabolism, also mediating proximal tubule recovery from kidney disease [47,48]. Spargel (Srl), the *Drosophila*

PGC1α ortholog, regulates mitochondrial activity and it functions redundantly with the GABPA ortholog Ets97D/Delg to promote mitochondrial biogenesis [49,50]. Furthermore, Srl overexpression is known to counteract HFD-induced dysfunction of the *Drosophila* heart [51]. Using nephrocyte-specific RNAi knockdowns, we found that *Srl* and *Delg* are each required for the normal mitochondrial volume of STD nephrocytes (**S5A Fig)**. Importantly, knockdown of *PGC1α/Srl* also decreased *ATGL-GFP* expression in STD nephrocytes (**Fig 6D**). This finding shows that a key transcriptional coactivator of mitochondrial genes, PGC1α, is required directly or indirectly to regulate the expression of the *ATGL* gene.

To define the role of PGC1α/Srl in HFD nephrocyte dysfunction, we used both pharmacological and genetic approaches. Pyrroloquinoline quinone (PQQ), an indirect activator of PGC1α/Srl [52,53], was able to restore substantially the mitochondrial volume of control or DGAT1[i] HFD nephrocytes (**Fig 6E**). Strikingly, the degree of rescue of HFD mitochondrial volume with PQQ was comparable to that achieved via ATGL expression (**Fig 6E**). The PQQ experiments rule out that PGC1α solely acts upstream of DGAT1-dependent triglyceride biosynthesis and, together with the *GFP* reporter analysis, suggest that a HFD-induced decrease in PGC1α expression/activity could downregulate *ATGL* gene expression. Importantly, genetic knockdown of *PGC1α/Srl*, or *Delg*, inhibited ATGL rescue of HFD nephrocyte mitochondrial volume (**Fig 6F**). *Srl* knockdown also completely blocked ATGL rescue of nephrocyte dextran uptake, which remained at or slightly below the level that is observed in control genotype HFD animals (**Fig 6G and S5B Fig**). These pharmacological and genetic experiments together demonstrate that PGC1α is required for the ATGL rescue of HFD-induced deficits in nephrocyte mitochondria and endocytosis.

Fig 6: Rescue of nephrocyte mitochondria and endocytosis on HFD requires PGC1α/Srl.
(**A-D**) Confocal micrographs of nephrocytes and quantifications showing that *ATGL-GFP* reporter expression is suppressed by HFD (A-B), restored by *Dot>ATGL* (C), and decreased by *Dot>Srl[i]* on STD diet (D). Note that the GFP intensities of HFD and STD nephrocytes can be directly compared in panel A because they are both imaged within the same field of view.
(**E**) Dietary supplementation with pyrroloquinoline quinone (PQQ) rescues nephrocyte mitochondrial volume on HFD, in control or *Dot>DGAT1[i]* genotypes, back to a value similar to that in HFD *Dot>ATGL* or STD larvae.
(**F**) *Dot>ATGL* rescue of nephrocyte mitochondrial volume is compromised by simultaneous knockdown of *PGC1α* (*Dot>ATGL;Srl[i]*) or Delg (*Dot>ATGL;Delg[i]*).
(**G**) *Dot>ATGL* rescue of 10 kDa and 500 kDa dextran uptake on HFD is blocked by simultaneous knockdown of *PGC1α* (*Dot>ATGL;Srl[i]*).

Discussion

This study establishes the first *Drosophila* model for high-fat diet induced CKD. Our results reveal that exposure to HFD induces renal defects in *Drosophila* that are strikingly similar to those observed in mammals. Key metabolic features of CKD in podocytes and proximal tubule cells are recapitulated in *Drosophila* nephrocytes including lipid droplet induction, a decrease in mitochondrial volume, as well as compromised endocytic uptake of albumin and other macromolecules. The powerful genetics and high-throughput possibilities of the *Drosophila* model open up a significant new avenue for *in vivo* mechanistic studies of CKD. We now discuss the mechanism by which HFD induces CKD-like dysfunction in *Drosophila* and how increased ATGL/Bmm expression rescues it. We also discuss how side-by-side functional comparisons of the triglyceride metabolic enzymes DGAT1 and ATGL provide a widely applicable strategy for clarifying the cellular functions of stress-induced lipid droplets.

Boosting fatty acid flux through the triglyceride compartment protects renal endocytosis

ATGL overexpression is predicted to increase the release of free fatty acids, a change that is associated with lipotoxicity. Nevertheless, we find that the outcome of this genetic manipulation can either be beneficial or harmful for renal endocytosis, depending upon whether it is adipose or nephrocyte specific. We showed that HFD induction of lipid droplets and endocytic dysfunction in nephrocytes are both mimicked on STD via overexpression of ATGL in adipose tissue. Furthermore, HFD induction of nephrocyte lipid droplets requires the Cubilin endocytic receptor. Together, these results suggest that excess diet-derived fatty acids are mobilised from adipose tissue into the circulation, taken up by nephrocytes via receptor-mediated endocytosis, and subsequently accumulate in the core of lipid droplets.

A key finding of this study is that experimentally boosting the expression of ATGL in nephrocytes rescues most of the deleterious effects of HFD on the morphology and function of these cells. Thus, ATGL expression substantially restored ER volume, mitochondrial volume, endosomal number and, importantly, the endocytosis of dextran and albumin. This striking protection of nephrocyte endocytic function by ATGL is strictly dependent upon DGAT1, strongly suggesting that it requires fatty acid flux into and out of the lipid droplet triglyceride compartment. Our analysis also suggests that fatty acid flux through the triglyceride compartment is suboptimal on HFD because ATGL becomes limiting. The observation that HFD decreases nephrocyte *ATGL* reporter expression is indicative of repression at the

transcriptional level. However, our results do not rule out an additional contribution to HFD repression of ATGL from post-transcriptional mechanisms.

A general strategy for distinguishing between different lipid droplet functions

Our systematic comparisons between two different genetic methods for inhibiting stress-induced lipid droplets have important implications for interpreting the role of these organelles in a wide range of different biological contexts. In the case of nephrocytes, we have shown that either blocking the last step of triglyceride synthesis (DGAT1 knockdown) or boosting lipolysis (ATGL overexpression) efficiently prevent the accumulation of lipid droplets, yet these manipulations produce different functional outcomes. We now outline how side-by-side comparisons of both genetic perturbations can be used to distinguish whether lipid droplets are harmful or protective and, if they are protective, to identify the underlying mechanism. DGAT1 knockdown in HFD nephrocytes increases lipid peroxidation damage and decreases endocytosis. Hence, as for the hypoxic CNS [54], synthesis of the triglyceride core of the lipid droplet has a net protective effect on nephrocytes. To determine how the triglyceride core protects, it is then important to consider the functional effect of boosting lipolysis via ATGL. A harmful outcome implies that the protection offered by the lipid droplet triglyceride core involves sequestration of potentially toxic lipids [54], whereas a beneficial effect suggests that it corresponds to the release of protective lipids, with signalling or other roles [19,55,56]. In the case of HFD nephrocytes, we found that boosting ATGL rescues macromolecular uptake, suggesting that nephrocyte lipid droplets protect by acting as a source of beneficial lipids. Similar reasoning suggests a reinterpretation of two previous studies in the adult *Drosophila* retina, which reported that glial lipid droplets induced either by mitochondrial defects or by loss of ADAM17 metalloprotease act to promote neurodegeneration [57,58]. This conclusion was based on evidence that decreasing lipid droplets via the overexpression of Bmm/ATGL leads to less neurodegeneration. Our DGAT1 and ATGL comparisons now provide evidence that boosting ATGL equates to a gain not a loss of function for lipid droplets, or more precisely for their role as a platform for triglyceride lipolysis. Therefore, the previous retinal studies and our own nephrocyte findings are consistent in demonstrating a beneficial role for the lipolysis function of lipid droplets. This illustrates that caution is needed when assigning protective or harmful roles to lipid droplets and argues for a more nuanced interpretation that parses their various subfunctions.

ATGL rescues renal endocytic dysfunction via the PGC1α pathway

This study reveals that ATGL/Bmm rescues HFD-induced dysfunction in *Drosophila* renal cells via a mechanism that requires GABPA/Delg and also PGC1α/Srl, a conserved regulator of mitochondrial biogenesis, membrane potential and ß-oxidation [47,48]. A pharmacological approach provided evidence that PGC1α is sufficient to correct HFD deficits in nephrocyte mitochondrial volume. Unlike ATGL rescue, PGC1α rescue does not require DGAT1-dependent triglyceride synthesis. Moreover, genetic epistasis tests demonstrated that PGC1α is necessary for ATGL to rescue both the mitochondrial volume and the endocytic dysfunction of HFD nephrocytes. These findings together make it likely that triglyceride synthesis and ATGL-dependent lipolysis act upstream of the PGC1α-dependent mitochondrial processes required for optimal nephrocyte endocytosis. Nevertheless, there is transgenic reporter evidence for the reverse regulatory relationship, namely that *PGC1α* is required for *ATGL* expression. It is therefore probable that there is bidirectional positive regulation between ATGL and PGC1α, which is important for mitochondrial function and compromised by exposure to HFD. Reporter experiments also showed that boosting ATGL activity increases *ATGL* transcription, thus suggesting the existence of an ATGL positive feedback loop. Even though the complete molecular pathways accounting for how increased ATGL expression in HFD nephrocytes rescues PGC1α mitochondrial processes are not yet known, it is plausible that ATGL activates transcription factors cooperating with the PGC1α coactivator. For example, it has been reported that mammalian ATGL releases lipolytic products that can activate the nuclear receptor PPARα, a partner of PGC1α, either directly or via the Sirtuin 1 deacetylase [59,60]. Another non-mutually exclusive possibility is that ATGL could rescue HFD nephrocytes via channelling fatty acids from lipid droplets into mitochondria for ß-oxidation, as has been suggested in cultured cells subject to nutrient deprivation or fatty acid toxicity [55,61]. In the context of CKD, it is known that ß-oxidation is downregulated and the pharmacological reversal of this has been proposed as a potential treatment [62]. Our findings now raise the possibility that pharmacological activators of lipid droplet lipolysis could be a useful addition to existing treatments for CKD. For example, small-molecule ligands for a potent activator of ATGL can boost lipolysis in adipose and muscle tissue and it has been argued that they might be developed into therapeutic entities for obesity and diabetes [63]. In the context of CKD, our nephrocyte study suggests that it will be important to test whether this approach has the ability to induce enough beneficial lipolysis in renal cells to deal with the concomitant increase in lipid overflow from adipose tissue. If this is the case, then therapies boosting lipid droplet lipolysis could provide a novel strategy for targeting obesity-associated CKD as well as its comorbidities.

Materials and Methods

Drosophila strains

Control *Drosophila* strains used in this study, including controls for Gal4/UAS experiments, were a *Wolbachia*-negative derivative of the w^{1118} iso^{31} strain [64] and/or *UAS-mCherry RNAi* (y^1 *sc** v^1 sev^{21}*; P{y[+t7.7] v[+t1.8]=VALIUM20-mCherry}attP2*). Nephrocyte and fat-body specific manipulations were performed using *Dot-GAL4* [65] and *Lpp-GAL4* [66] respectively. The following UAS fly stocks were used in this study and previously validated in the associated references: *UAS-Cubn*[i] (w^{1118}*; P{GD6458}v14613*) [67], *UAS-mdy[i]* (*P{KK102899}VIE-260B*) [54], *UAS-bmm* [44], *Rab7::YFPmyc* [39], *UAS-LDAH::eGFP* (*UAS-CG9186::eGFP*) [37], and *UAS-Delg[i]* (y^1 v^1*; P{y[+t7.7] v[+t1.8]=TRiP.JF01805}attP2*). Similar results were obtained using *UAS-Srl[i]* (*P{KK100201}VIE-260B*) [53] or *UAS-Srl[i]* (y^1 *sc** v^1 sev^{21}*; P{y[+t7.7] v[+t1.8]=TRiP.HMS00858}attP2*) [68].

Standard and high fat diet, larval staging and PQQ treatment

All stocks were raised on our standard diet (STD) at 25°C unless otherwise stated. STD contains 58.5 g/L glucose, 6.63 g/L cornmeal, 23.4 g/L dried yeast, 7.02 g/L agar, 1.95 g/L Nipagen and 7.8 mg/L Bavistan, unless specified otherwise. Flies were left to lay eggs for 2 hr, on plates containing grape juice agar with yeast paste in the centre. After egg maturation for 24 hr, hatched L1 larvae were collected from the agar plates during a 1 hr time window using blunt forceps, 20-25 individuals transferred to each vial at 25°C with the appropriate diet and raised to wandering L3 stage (~90 hr after larval hatching) for nephrocyte analysis. High fat diet (HFD) corresponds to STD supplemented with 20 mM oleic acid. Pyrroloquinoline quinone (PQQ) as added to the diet at 0.3 mM.

Immunostaining and confocal microscopy

Larvae were inverted and fixed in 4% PFA in PBS for 30 minutes at 25°C. After fixation, samples were washed three times in PBS and dissected further, if necessary. Samples were blocked in 10% normal goat serum (NGS) in PBS + 0.2% Triton (PBT), incubated overnight at 4°C with primary antibodies diluted in 10% NGS in PBT, washed three times in PBT over 1 hr, incubated overnight at 4°C with secondary antibodies diluted in 10% NGS in PBT, and then washed three times in PBT over 1 hr. Primary antibodies used were chicken anti-GFP at 1:1000 (Abcam, ab13970), rat anti-KDEL 10C3 at 1:300 (Abcam, ab12223) and mouse anti-ATP5A 15H4C4 at 1:100 (Abcam, ab14748), the secondary antibodies were Alexa Fluor conjugated antibodies (ThermoFisher Scientific) used at concentration 1:500. For neutral lipid staining,

larvae were inverted in PBS and fixed overnight at 4°C in 2% PFA in PBL (75mM lysine, 37mM sodium phosphate buffer at pH7.4). Pericardial nephrocytes were dissected further in PBS, permeabilized for 4 min in 0.1% PBT, washed 3 times for 10 min in PBS, and stained with LipidTox Deep Red o/n at 4°C. All samples were mounted in Vectashield. For volume measurements, samples were mounted in a well generated by 1 layer of magic tape (Scotch) to avoid compression. All samples were imaged on a Leica SP5 upright microscope using oil immersion objectives. Samples for direct quantitative comparison were imaged on the same day using the same settings. For volume measurements, confocal Z stacks spanning the entire depth of the tissue were acquired (step size of 1 um) and analyses were carried out using Volocity v6 (Quorum Technologies).

ex vivo nephrocyte uptake assays

Dextran uptake assays were performed as described [31] with some modifications. Wandering L3 larvae were inverted in Schneider's Insect Medium, excess tissue was removed and larval carcasses with CNS and pericardial nephrocytes attached were incubated for 30 min at 25°C in Schneider's Medium with 10 kDa AlexaFluor568-dextran and 500 kDa FITC-dextran at a concentration of 0.33 mg/ml. For albumin uptake assay, pericardial nephrocytes were incubated for 30 min at 25°C in Schneider's Medium (S0146, Merck) with FITC-albumin and Red DQ-albumin at a concentration of 0.1 mg/ml. Next, tissues were washed with ice-cold PBS and fixed with 4% formaldehyde for 20 min at RT. If neutral lipid staining was required, tissues were permeabilised with 0.1% PBT for 5 min at RT, washed extensively with PBS and stained with LipidTox 633 o/n at 4°C. For BODIPY FL C12 (Thermo Fisher Scientific, D3822) uptake assays, pericardial nephrocytes were incubated for 30 min at 25°C in Schneider's Medium with 0.5 mg/ml delipidated BSA (A9205, Merck) and 10 µM BODIPY FL C12 green fluorescent fatty acid. Tissues were then washed with ice-cold PBS and fixed with 4% formaldehyde for 20 min at 25°C. Stained tissues were mounted in Vectashield on glass slides with a coverslip spacer of one layer of Scotch tape, and imaged on a Leica SP5 as described above.

Lipid peroxidation assay

To detect lipid peroxidation in nephrocytes, nephrocytes were dissected in Schneider's medium and incubated for 30 min in Schneider's medium containing 10% NGS and 2 µM BODIPY 581/591 C11 (Invitrogen, D3861). Samples were washed and mounted in Schneider's medium, then control and experimental samples were imaged sequentially for the non-oxidized (excitation: 561 nm, emission: 570-610 nm) and oxidized (excitation: 488 nm, emission: 500-

540 nm) forms. The oxidized: non-oxidized ratio was measured in each nephrocyte and intensity modulated ratiometric images were generated using Volocity v6 (Quorum Technologies).

Electron microscopy

For correlative light-electron microscopy (CLEM), dextran uptake assays were performed on dorsal vessel-pericardial nephrocyte complexes from STD and HFD larvae as described above. After washing in cold PBS, tissues were fixed with 4% paraformaldehyde in phosphate buffer (PB) for 1hr and flat mounted in 1.5% low-melting-temperature agarose in PB on glass coverslips. Rab7::YFP^{myc} expressing nephrocytes were imaged on a Zeiss LSM880 Airyscan confocal microscope using a 63x 1.4 NA oil immersion objective. Z stacks were obtained at 0.5 µm step size using Auto Z Brightness Correction. Airyscan processing was performed using default settings in the ZEN software. Samples were then removed from the glass slide, excess agarose trimmed off and postfixed with 2% paraformaldehyde and 2.5% glutaraldehyde for 1hr, prior to serial block face scanning electron microscopy (SBF SEM).

For SBF SEM, nephrocytes dissected from *Dot>DGAT1[i]* and *Dot>ATGL* larvae were first subjected to dextran uptake assays and representative cells then selected for SBF SEM analysis. Nephrocytes were then fixed with 2% or 4% paraformaldehyde and 2.5% glutaraldehyde in PB for 1h, washed in PB, and flat mounted in 1.5% low-melting-temperature agarose in PB on glass coverslips. All samples, including those for CLEM, were processed for SBF SEM using the previously described protocol with modifications [69]. Briefly, tissues were post-fixed in 2% osmium tetroxide and 1.5% potassium ferricyanide for 1hr, incubated in 1% thiocarbohydrazide for 20 min, followed by 2% osmium tetroxide for 30 min. Osmicated tissues were then stained *en bloc* with 1% uranyl acetate overnight, followed by Walton's lead aspartate staining for 30 min at 40–60°C. Tissues were then dehydrated with a graded ethanol series, flat-embedded in Durcupan ACM® resin, and polymerized at 60°C. Samples were mounted onto aluminum pins using conductive epoxy glue (ITW Chemtronics) and trimmed to the region of interest guided by light microscopy images. Trimmed blocks were sputter-coated with 5–10 nm platinum using a Q150R S sputter coater (Quorum Tech). SBF SEM data was collected using a 3View2XP (Gatan, Pleasanton, CA) attached to a Sigma VP SEM (Zeiss, Cambridge). The microscope was operated at 2.0-2.3kV with 30-µm aperture, using Variable Pressure mode or Focal Charge Compensation mode [70]. Inverted backscattered electron images were acquired through entire nephrocytes every 50 or 100 nm, at a resolution of 6.5–8.0 nm/pixel. Acquired images were imported into Fiji [71] and aligned using the Register Virtual Stack Slices [72].

For the Movies S1–S4, aligned data were scaled down to 50 nm/pixel and encoded into the H. 264 compression format using the ImageJ plugin imagej-ffmpeg-recorder.

SBF SEM quantification of endosomes

CLEM was used to define the morphology of the endocytic compartments to be quantified using SBF SEM. The Airyscan Z-stack was matched to the SBF SEM data using the Fiji plugin BigWarp. Endolysosomes were manually selected in each stack as landmarks, and thin-plate spline transformation was applied to match the two stacks. ~70 endolysosomes were classified using CLEM into five morphology groups based on their SEM luminal density and their Dextran and Rab7::YFP^{myc} status in the corresponding Airyscan images (**S3A Fig**). Dark endolysosomes with a luminal density similar to or higher than the cytoplasm were all Dextran$^-$ (but Rab7$^+$ and Rab7$^-$) and therefore, along with Golgi apparatus associated vesicles, were not segmented in SBF SEM images. White and light endosomes were segmented on one or more SBF SEM slices including the midplane of the compartment by fitting the largest inscribed circle using the Fiji plugin TrakEM2 [73]. Then using the Fiji 3D Object Counter [74], the size of the bounding box was used to estimate the object diameter and this was used to calculate the spherical volume. For quantitation of endosome numbers and volumes, a size threshold of 300 nm diameter was selected and validated by showing that it gave comparable endosome size distributions for the different fixation protocols used for CLEM or for standard SBF SEM (**S3B Fig**).

Statistical Analysis

R version 3.5.1 (2018-07-02) was used for all statistical analysis (R Core Team, 2018). Boxplots were generated using ggplot2, show the median with first and third quartile, and whiskers extend from the hinge by 1.5x inter-quartile range. Data points are coloured according to which independent experiment they are from. For statistical analyses, the data was modelled using a linear mixed model (LMM) with diet as fixed and independent experiment as random effect followed by a Wald Chi-Squared test. Asterisks show statistical significance (* $p<0.05$, ** $p<0.005$, ***$p<0.0005$). The data were modelled using restricted maximum likelihood (REML) linear mixed models (LMM) or general linear mixed models (GLMM) from the lme4 package [75]. The model fit was evaluated using normal quantile-quantile plots. Experimental manipulation such as diet, genetic manipulation and dextran size were categorized as fixed effects, and independent experiments were categorized as random effects. Statistical inference for fixed effects was tested by Wald Chi-Square test from the R car package [76]. For multiple

589 comparisons, estimated marginal means (EMM) were predicted using the R emmeans package
590 [77] and comparisons used Bonferroni correction. Statistical methods, parameters and results
591 for each figure are summarized in **Table S1**.
592

Acknowledgements

We acknowledge Mathias Beller, R. Kühnlein, and the late Susan Abmayr and Suzanne Eaton for fly stocks and antibodies. Fly stocks were also obtained from the Bloomington *Drosophila* Stock Center (NIH P40OD018537), the Vienna Drosophila Research Centre and the Kyoto *Drosophila* Genetic Resource. We thank Andrew Bailey, Clare Newell and Ian McGough for assistance with experiments as well as for helpful advice and discussions. We also thank Eva Islimye and Elisabeth Kamper for comments on the manuscript.

This work was supported by an Investigator Award to APG from the Wellcome Trust (104566/Z/14/Z) and by funding to APG from the Francis Crick Institute, which receives its core funding from Cancer Research UK (FC001088), the UK Medical Research Council (FC001088) and the Wellcome Trust (FC001088).

References

1. Alicic RZ, Rooney MT, Tuttle KR. Diabetic Kidney Disease: Challenges, Progress, and Possibilities. Clin J Am Soc Nephrol. 2017;12(12):2032-45. Epub 2017/05/20. doi: 10.2215/CJN.11491116. PubMed PMID: 28522654; PubMed Central PMCID: PMCPMC5718284.

2. Anders HJ, Huber TB, Isermann B, Schiffer M. CKD in diabetes: diabetic kidney disease versus nondiabetic kidney disease. Nat Rev Nephrol. 2018;14(6):361-77. Epub 2018/04/15. doi: 10.1038/s41581-018-0001-y. PubMed PMID: 29654297.

3. Carobbio S, Pellegrinelli V, Vidal-Puig A. Adipose Tissue Function and Expandability as Determinants of Lipotoxicity and the Metabolic Syndrome. Adv Exp Med Biol. 2017;960:161-96. Epub 2017/06/07. doi: 10.1007/978-3-319-48382-5_7. PubMed PMID: 28585199.

4. Escasany E, Izquierdo-Lahuerta A, Medina-Gomez G. Underlying Mechanisms of Renal Lipotoxicity in Obesity. Nephron. 2019;143(1):28-32. Epub 2019/01/10. doi: 10.1159/000494694. PubMed PMID: 30625473.

5. Moorhead JF, Chan MK, El-Nahas M, Varghese Z. Lipid nephrotoxicity in chronic progressive glomerular and tubulo-interstitial disease. Lancet. 1982;2(8311):1309-11. Epub 1982/12/11. doi: 10.1016/s0140-6736(82)91513-6. PubMed PMID: 6128601.

6. Krahmer N, Farese RV, Jr., Walther TC. Balancing the fat: lipid droplets and human disease. EMBO Mol Med. 2013;5(7):973-83. Epub 2013/06/07. doi: 10.1002/emmm.201100671. PubMed PMID: 23740690; PubMed Central PMCID: PMCPMC3721468.

7. Briffa JF, McAinch AJ, Poronnik P, Hryciw DH. Adipokines as a link between obesity and chronic kidney disease. Am J Physiol Renal Physiol. 2013;305(12):F1629-36. Epub 2013/10/11. doi: 10.1152/ajprenal.00263.2013. PubMed PMID: 24107418.

8. Zhu Q, Scherer PE. Immunologic and endocrine functions of adipose tissue: implications for kidney disease. Nat Rev Nephrol. 2018;14(2):105-20. Epub 2017/12/05. doi: 10.1038/nrneph.2017.157. PubMed PMID: 29199276.

9. D'Agati VD, Chagnac A, de Vries AP, Levi M, Porrini E, Herman-Edelstein M, et al. Obesity-related glomerulopathy: clinical and pathologic characteristics and pathogenesis. Nat Rev Nephrol. 2016;12(8):453-71. Epub 2016/06/07. doi: 10.1038/nrneph.2016.75. PubMed PMID: 27263398.

10. Jiang T, Wang Z, Proctor G, Moskowitz S, Liebman SE, Rogers T, et al. Diet-induced obesity in C57BL/6J mice causes increased renal lipid accumulation and glomerulosclerosis via a sterol regulatory element-binding protein-1c-dependent pathway. J Biol Chem. 2005;280(37):32317-25. Epub 2005/07/28. doi: 10.1074/jbc.M500801200. PubMed PMID: 16046411.

643 11. Li C, Lin Y, Luo R, Chen S, Wang F, Zheng P, et al. Intrarenal renin-angiotensin
644 system mediates fatty acid-induced ER stress in the kidney. Am J Physiol Renal Physiol.
645 2016;310(5):F351-63. Epub 2015/12/18. doi: 10.1152/ajprenal.00223.2015. PubMed PMID:
646 26672616; PubMed Central PMCID: PMCPMC4971807.

647 12. Kuwahara S, Hosojima M, Kaneko R, Aoki H, Nakano D, Sasagawa T, et al. Megalin-
648 Mediated Tubuloglomerular Alterations in High-Fat Diet-Induced Kidney Disease. J Am Soc
649 Nephrol. 2016;27(7):1996-2008. Epub 2015/11/05. doi: 10.1681/ASN.2015020190. PubMed
650 PMID: 26534923; PubMed Central PMCID: PMCPMC4926965.

651 13. Szeto HH, Liu S, Soong Y, Alam N, Prusky GT, Seshan SV. Protection of
652 mitochondria prevents high-fat diet-induced glomerulopathy and proximal tubular injury.
653 Kidney Int. 2016;90(5):997-1011. Epub 2016/08/16. doi: 10.1016/j.kint.2016.06.013.
654 PubMed PMID: 27519664.

655 14. Forbes JM, Thorburn DR. Mitochondrial dysfunction in diabetic kidney disease. Nat
656 Rev Nephrol. 2018;14.

657 15. Welte MA, Gould AP. Lipid droplet functions beyond energy storage. Biochim
658 Biophys Acta Mol Cell Biol Lipids. 2017;1862(10 Pt B):1260-72. Epub 2017/07/25. doi:
659 10.1016/j.bbalip.2017.07.006. PubMed PMID: 28735096; PubMed Central PMCID:
660 PMCPMC5595650.

661 16. Olzmann JA, Carvalho P. Dynamics and functions of lipid droplets. Nat Rev Mol Cell
662 Biol. 2019;20(3):137-55. Epub 2018/12/14. doi: 10.1038/s41580-018-0085-z. PubMed PMID:
663 30523332; PubMed Central PMCID: PMCPMC6746329.

664 17. Walther TC, Chung J, Farese RV, Jr. Lipid Droplet Biogenesis. Annu Rev Cell Dev
665 Biol. 2017;33:491-510. Epub 2017/08/11. doi: 10.1146/annurev-cellbio-100616-060608.
666 PubMed PMID: 28793795.

667 18. Henne WM, Reese ML, Goodman JM. The assembly of lipid droplets and their roles
668 in challenged cells. EMBO J. 2018;37(12). Epub 2018/05/24. doi: 10.15252/embj.201898947.
669 PubMed PMID: 29789390; PubMed Central PMCID: PMCPMC6003646.

670 19. Zechner R, Zimmermann R, Eichmann TO, Kohlwein SD, Haemmerle G, Lass A, et
671 al. FAT SIGNALS--lipases and lipolysis in lipid metabolism and signaling. Cell Metab.
672 2012;15(3):279-91. Epub 2012/03/13. doi: 10.1016/j.cmet.2011.12.018. PubMed PMID:
673 22405066; PubMed Central PMCID: PMCPMC3314979.

674 20. Schulze RJ, Sathyanarayan A, Mashek DG. Breaking fat: The regulation and
675 mechanisms of lipophagy. Biochim Biophys Acta Mol Cell Biol Lipids. 2017;1862(10 Pt
676 B):1178-87. Epub 2017/06/24. doi: 10.1016/j.bbalip.2017.06.008. PubMed PMID: 28642194;
677 PubMed Central PMCID: PMCPMC5595645.

678 21. Kimmelstiel P, Wilson C. Intercapillary Lesions in the Glomeruli of the Kidney. Am J
679 Pathol. 1936;12(1):83-98 7. Epub 1936/01/01. PubMed PMID: 19970254; PubMed Central
680 PMCID: PMCPMC1911022.

681 22. Herman-Edelstein M, Scherzer P, Tobar A, Levi M, Gafter U. Altered renal lipid
682 metabolism and renal lipid accumulation in human diabetic nephropathy. J Lipid Res.
683 2014;55(3):561-72. Epub 2013/12/29. doi: 10.1194/jlr.P040501. PubMed PMID: 24371263;
684 PubMed Central PMCID: PMCPMC3934740.

685 23. Chen W, Zhang Q, Cheng S, Huang J, Diao G, Han J. Atgl gene deletion predisposes
686 to proximal tubule damage by impairing the fatty acid metabolism. Biochem Biophys Res
687 Commun. 2017;487(1):160-6. Epub 2017/04/13. doi: 10.1016/j.bbrc.2017.03.170. PubMed
688 PMID: 28400046.

689 24. Chen W, Jiang Y, Han J, Hu J, He T, Yan T, et al. Atgl deficiency induces podocyte
690 apoptosis and leads to glomerular filtration barrier damage. FEBS J. 2017;284(7):1070-81.
691 Epub 2017/02/15. doi: 10.1111/febs.14038. PubMed PMID: 28194887.

692 25. Ugur B, Chen K, Bellen HJ. Drosophila tools and assays for the study of human
693 diseases. Dis Model Mech. 2016;9(3):235-44. Epub 2016/03/05. doi: 10.1242/dmm.023762.
694 PubMed PMID: 26935102; PubMed Central PMCID: PMCPMC4833332.

695 26. Denholm B, Skaer H. Bringing together components of the fly renal system. Curr
696 Opin Genet Dev. 2009;19(5):526-32. Epub 2009/09/29. doi: 10.1016/j.gde.2009.08.006.
697 PubMed PMID: 19783135; PubMed Central PMCID: PMCPMC2789252.

698 27. Dow JA, Romero MF. Drosophila provides rapid modeling of renal development,
699 function, and disease. Am J Physiol Renal Physiol. 2010;299(6):F1237-44. Epub 2010/10/12.
700 doi: 10.1152/ajprenal.00521.2010. PubMed PMID: 20926630; PubMed Central PMCID:
701 PMCPMC3006309.

702 28. Na J, Cagan R. The Drosophila nephrocyte: back on stage. J Am Soc Nephrol.
703 2013;24(2):161-3. Epub 2013/01/22. doi: 10.1681/ASN.2012121227. PubMed PMID:
704 23334393.

705 29. O'Donnell MJ, Maddrell SH. Fluid reabsorption and ion transport by the lower
706 Malpighian tubules of adult female Drosophila. J Exp Biol. 1995;198(Pt 8):1647-53. Epub
707 1995/08/01. PubMed PMID: 7636442.

708 30. Cabrero P, Terhzaz S, Dornan AJ, Ghimire S, Holmes HL, Turin DR, et al.
709 Specialized stellate cells offer a privileged route for rapid water flux in Drosophila renal
710 tubule. Proc Natl Acad Sci U S A. 2020;117(3):1779-87. Epub 2020/01/08. doi:
711 10.1073/pnas.1915943117. PubMed PMID: 31907321; PubMed Central PMCID:
712 PMCPMC6983416.

713 31. Weavers H, Prieto-Sanchez S, Grawe F, Garcia-Lopez A, Artero R, Wilsch-
714 Brauninger M, et al. The insect nephrocyte is a podocyte-like cell with a filtration slit
715 diaphragm. Nature. 2009;457(7227):322-6. Epub 2008/10/31. doi: 10.1038/nature07526.
716 PubMed PMID: 18971929; PubMed Central PMCID: PMCPMC2687078.

717 32. Zhuang S, Shao H, Guo F, Trimble R, Pearce E, Abmayr SM. Sns and Kirre, the
718 Drosophila orthologs of Nephrin and Neph1, direct adhesion, fusion and formation of a slit
719 diaphragm-like structure in insect nephrocytes. Development. 2009;136(14):2335-44. Epub
720 2009/06/12. doi: 10.1242/dev.031609. PubMed PMID: 19515699; PubMed Central PMCID:
721 PMCPMC2729346.

722 33. Zhang F, Zhao Y, Chao Y, Muir K, Han Z. Cubilin and amnionless mediate protein
723 reabsorption in Drosophila nephrocytes. J Am Soc Nephrol. 2013;24(2):209-16. Epub
724 2012/12/25. doi: 10.1681/ASN.2012080795. PubMed PMID: 23264686; PubMed Central
725 PMCID: PMCPMC3559489.

726 34. Hermle T, Braun DA, Helmstadter M, Huber TB, Hildebrandt F. Modeling
727 Monogenic Human Nephrotic Syndrome in the Drosophila Garland Cell Nephrocyte. J Am
728 Soc Nephrol. 2017;28(5):1521-33. Epub 2016/12/10. doi: 10.1681/ASN.2016050517.
729 PubMed PMID: 27932481; PubMed Central PMCID: PMCPMC5407722.

730 35. Marchesin V, Perez-Marti A, Le Meur G, Pichler R, Grand K, Klootwijk ED, et al.
731 Molecular Basis for Autosomal-Dominant Renal Fanconi Syndrome Caused by HNF4A. Cell
732 Rep. 2019;29(13):4407-21 e5. Epub 2019/12/26. doi: 10.1016/j.celrep.2019.11.066. PubMed
733 PMID: 31875549; PubMed Central PMCID: PMCPMC6941224.

734 36. Na J, Sweetwyne MT, Park AS, Susztak K, Cagan RL. Diet-Induced Podocyte
735 Dysfunction in Drosophila and Mammals. Cell Rep. 2015;12(4):636-47. Epub 2015/07/21.
736 doi: 10.1016/j.celrep.2015.06.056. PubMed PMID: 26190114; PubMed Central PMCID:
737 PMCPMC4532696.

738 37. Thiel K, Heier C, Haberl V, Thul PJ, Oberer M, Lass A, et al. The evolutionarily
739 conserved protein CG9186 is associated with lipid droplets, required for their positioning and
740 for fat storage. J Cell Sci. 2013;126(Pt 10):2198-212. Epub 2013/03/26. doi:
741 10.1242/jcs.120493. PubMed PMID: 23525007; PubMed Central PMCID:
742 PMCPMC3880856.

743 38. Kawasaki Y, Matsumoto A, Miyaki T, Kinoshita M, Kakuta S, Sakai T, et al. Three-
744 dimensional architecture of pericardial nephrocytes in Drosophila melanogaster revealed by
745 FIB/SEM tomography. Cell Tissue Res. 2019;378(2):289-300. Epub 2019/05/16. doi:
746 10.1007/s00441-019-03037-3. PubMed PMID: 31089884.

747 39. Dunst S, Kazimiers T, von Zadow F, Jambor H, Sagner A, Brankatschk B, et al.
748 Endogenously tagged rab proteins: a resource to study membrane trafficking in Drosophila.
749 Dev Cell. 2015;33(3):351-65. Epub 2015/05/06. doi: 10.1016/j.devcel.2015.03.022. PubMed
750 PMID: 25942626; PubMed Central PMCID: PMCPMC4431667.

751 40. Kosaka T, Ikeda K. Reversible blockage of membrane retrieval and endocytosis in the
752 garland cell of the temperature-sensitive mutant of Drosophila melanogaster, shibirets1. J Cell
753 Biol. 1983;97(2):499-507. Epub 1983/08/01. doi: 10.1083/jcb.97.2.499. PubMed PMID:
754 6411734; PubMed Central PMCID: PMCPMC2112522.

755 41. Koenig JH, Ikeda K. Transformational process of the endosomal compartment in
756 nephrocytes of Drosophila melanogaster. Cell Tissue Res. 1990;262(2):233-44. Epub
757 1990/11/01. doi: 10.1007/BF00309878. PubMed PMID: 2127554.

758 42. Lorincz P, Lakatos Z, Varga A, Maruzs T, Simon-Vecsei Z, Darula Z, et al.
759 MiniCORVET is a Vps8-containing early endosomal tether in Drosophila. Elife. 2016;5.
760 Epub 2016/06/03. doi: 10.7554/eLife.14226. PubMed PMID: 27253064; PubMed Central
761 PMCID: PMCPMC4935465.

762 43. Gutierrez E, Wiggins D, Fielding B, Gould AP. Specialized hepatocyte-like cells
763 regulate Drosophila lipid metabolism. Nature. 2007;445(7125):275-80. Epub 2006/12/01. doi:
764 10.1038/nature05382. PubMed PMID: 17136098.

765 44. Gronke S, Mildner A, Fellert S, Tennagels N, Petry S, Muller G, et al. Brummer lipase
766 is an evolutionary conserved fat storage regulator in Drosophila. Cell Metab. 2005;1(5):323-
767 30. Epub 2005/08/02. doi: 10.1016/j.cmet.2005.04.003. PubMed PMID: 16054079.

768 45. Eshbach ML, Weisz OA. Receptor-Mediated Endocytosis in the Proximal Tubule.
769 Annu Rev Physiol. 2017;79:425-48. Epub 2016/11/05. doi: 10.1146/annurev-physiol-022516-
770 034234. PubMed PMID: 27813828; PubMed Central PMCID: PMCPMC5512543.

771 46. Men TT, Thanh DN, Yamaguchi M, Suzuki T, Hattori G, Arii M, et al. A Drosophila
772 Model for Screening Antiobesity Agents. Biomed Res Int. 2016;2016:6293163. Epub
773 2016/06/02. doi: 10.1155/2016/6293163. PubMed PMID: 27247940; PubMed Central
774 PMCID: PMCPMC4876200.

775 47. Spiegelman BM. Transcriptional control of mitochondrial energy metabolism through
776 the PGC1 coactivators. Novartis Found Symp. 2007;287:60-3; discussion 3-9. Epub
777 2007/12/14. PubMed PMID: 18074631.

778 48. Bhargava P, Schnellmann RG. Mitochondrial energetics in the kidney. Nat Rev
779 Nephrol. 2017;13(10):629-46. Epub 2017/08/15. doi: 10.1038/nrneph.2017.107. PubMed
780 PMID: 28804120; PubMed Central PMCID: PMCPMC5965678.

781 49. Tiefenbock SK, Baltzer C, Egli NA, Frei C. The Drosophila PGC-1 homologue
782 Spargel coordinates mitochondrial activity to insulin signalling. EMBO J. 2010;29(1):171-83.
783 Epub 2009/11/17. doi: 10.1038/emboj.2009.330. PubMed PMID: 19910925; PubMed Central
784 PMCID: PMCPMC2808377.

785 50. Baltzer C, Tiefenböck SK, Marti M, Frei C. Nutrition Controls Mitochondrial
786 Biogenesis in the Drosophila Adipose Tissue through Delg and Cyclin D/Cdk4. PLoS ONE.
787 2009;4(9). doi: 10.1371/journal.pone.0006935.

788 51. Diop SB, Bisharat-Kernizan J, Birse RT, Oldham S, Ocorr K, Bodmer R. PGC-
789 1/Spargel Counteracts High-Fat-Diet-Induced Obesity and Cardiac Lipotoxicity Downstream
790 of TOR and Brummer ATGL Lipase. Cell Rep. 2015;10(9):1572-84. Epub 2015/03/11. doi:
791 10.1016/j.celrep.2015.02.022. PubMed PMID: 25753422; PubMed Central PMCID:
792 PMCPMC4560688.

793 52. Saihara K, Kamikubo R, Ikemoto K, Uchida K, Akagawa M. Pyrroloquinoline
794 Quinone, a Redox-Active o-Quinone, Stimulates Mitochondrial Biogenesis by Activating the
795 SIRT1/PGC-1alpha Signaling Pathway. Biochemistry. 2017;56(50):6615-25. Epub
796 2017/12/01. doi: 10.1021/acs.biochem.7b01185. PubMed PMID: 29185343.

797 53. Ng CH, Basil AH, Hang L, Tan R, Goh KL, O'Neill S, et al. Genetic or
798 pharmacological activation of the Drosophila PGC-1alpha ortholog spargel rescues the
799 disease phenotypes of genetic models of Parkinson's disease. Neurobiol Aging. 2017;55:33-7.
800 Epub 2017/04/14. doi: 10.1016/j.neurobiolaging.2017.03.017. PubMed PMID: 28407521.

801 54. Bailey AP, Koster G, Guillermier C, Hirst EM, MacRae JI, Lechene CP, et al.
802 Antioxidant Role for Lipid Droplets in a Stem Cell Niche of Drosophila. Cell.
803 2015;163(2):340-53. Epub 2015/10/10. doi: 10.1016/j.cell.2015.09.020. PubMed PMID:
804 26451484; PubMed Central PMCID: PMCPMC4601084.

805 55. Nguyen TB, Louie SM, Daniele JR, Tran Q, Dillin A, Zoncu R, et al. DGAT1-
806 Dependent Lipid Droplet Biogenesis Protects Mitochondrial Function during Starvation-
807 Induced Autophagy. Dev Cell. 2017;42(1):9-21 e5. Epub 2017/07/12. doi:
808 10.1016/j.devcel.2017.06.003. PubMed PMID: 28697336; PubMed Central PMCID:
809 PMCPMC5553613.

56. Khan SA, Sathyanarayan A, Mashek MT, Ong KT, Wollaston-Hayden EE, Mashek DG. ATGL-catalyzed lipolysis regulates SIRT1 to control PGC-1alpha/PPAR-alpha signaling. Diabetes. 2015;64(2):418-26. Epub 2015/01/24. doi: 10.2337/db14-0325. PubMed PMID: 25614670; PubMed Central PMCID: PMCPMC4303962.

57. Liu L, Zhang K, Sandoval H, Yamamoto S, Jaiswal M, Sanz E, et al. Glial Lipid Droplets and ROS Induced by Mitochondrial Defects Promote Neurodegeneration. Cell. 2015;160(1-2):177-90. doi: 10.1016/j.cell.2014.12.019.

58. Muliyil S, Levet C, Düsterhöft S, Dulloo I, Cowley S, Freeman M. ADAM17-triggered TNF signalling protects the ageing Drosophila retina from lipid droplet mediated degeneration. bioRxiv. 2020:2020.01.09.900209. doi: 10.1101/2020.01.09.900209.

59. Haemmerle G, Moustafa T, Woelkart G, Buttner S, Schmidt A, van de Weijer T, et al. ATGL-mediated fat catabolism regulates cardiac mitochondrial function via PPAR-alpha and PGC-1. Nat Med. 2011;17(9):1076-85. Epub 2011/08/23. doi: 10.1038/nm.2439. PubMed PMID: 21857651; PubMed Central PMCID: PMCPMC3244833.

60. Najt CP, Khan SA, Heden TD, Witthuhn BA, Perez M, Heier JL, et al. Lipid Droplet-Derived Monounsaturated Fatty Acids Traffic via PLIN5 to Allosterically Activate SIRT1. Mol Cell. 2020;77(4):810-24 e8. Epub 2020/01/07. doi: 10.1016/j.molcel.2019.12.003. PubMed PMID: 31901447.

61. Rambold AS, Cohen S, Lippincott-Schwartz J. Fatty acid trafficking in starved cells: regulation by lipid droplet lipolysis, autophagy, and mitochondrial fusion dynamics. Dev Cell. 2015;32(6):678-92. Epub 2015/03/11. doi: 10.1016/j.devcel.2015.01.029. PubMed PMID: 25752962; PubMed Central PMCID: PMCPMC4375018.

62. Kang HM, Ahn SH, Choi P, Ko YA, Han SH, Chinga F, et al. Defective fatty acid oxidation in renal tubular epithelial cells has a key role in kidney fibrosis development. Nat Med. 2015;21(1):37-46. Epub 2014/11/25. doi: 10.1038/nm.3762. PubMed PMID: 25419705; PubMed Central PMCID: PMCPMC4444078.

63. Sanders MA, Madoux F, Mladenovic L, Zhang H, Ye X, Angrish M, et al. Endogenous and Synthetic ABHD5 Ligands Regulate ABHD5-Perilipin Interactions and Lipolysis in Fat and Muscle. Cell Metab. 2015;22(5):851-60. Epub 2015/09/29. doi: 10.1016/j.cmet.2015.08.023. PubMed PMID: 26411340; PubMed Central PMCID: PMCPMC4862007.

64. Stefana MI, Driscoll PC, Obata F, Pengelly AR, Newell CL, MacRae JI, et al. Developmental diet regulates Drosophila lifespan via lipid autotoxins. Nat Commun. 2017;8(1):1384. Epub 2017/11/11. doi: 10.1038/s41467-017-01740-9. PubMed PMID: 29123106; PubMed Central PMCID: PMCPMC5680271.

65. Kimbrell DA, Hice C, Bolduc C, Kleinhesselink K, Beckingham K. The Dorothy enhancer has Tinman binding sites and drives hopscotch-induced tumor formation. Genesis. 2002;34(1-2):23-8. Epub 2002/09/27. doi: 10.1002/gene.10134. PubMed PMID: 12324942.

66. Brankatschk M, Eaton S. Lipoprotein particles cross the blood-brain barrier in Drosophila. J Neurosci. 2010;30(31):10441-7. Epub 2010/08/06. doi: 10.1523/JNEUROSCI.5943-09.2010. PubMed PMID: 20685986.

851 67. Zhang F, Zhao Y, Han Z. An in vivo functional analysis system for renal gene
852 discovery in Drosophila pericardial nephrocytes. J Am Soc Nephrol. 2013;24(2):191-7. Epub
853 2013/01/08. doi: 10.1681/ASN.2012080769. PubMed PMID: 23291470; PubMed Central
854 PMCID: PMCPMC3559487.

855 68. Merzetti EM, Staveley BE. spargel, the PGC-1alpha homologue, in models of
856 Parkinson disease in Drosophila melanogaster. BMC Neurosci. 2015;16:70. Epub 2015/10/28.
857 doi: 10.1186/s12868-015-0210-2. PubMed PMID: 26502946; PubMed Central PMCID:
858 PMCPMC4623274.

859 69. Russell MR, Lerner TR, Burden JJ, Nkwe DO, Pelchen-Matthews A, Domart MC, et
860 al. 3D correlative light and electron microscopy of cultured cells using serial blockface
861 scanning electron microscopy. J Cell Sci. 2017;130(1):278-91. Epub 2016/07/23. doi:
862 10.1242/jcs.188433. PubMed PMID: 27445312; PubMed Central PMCID:
863 PMCPMC5394779.

864 70. Deerinck TJ, Shone TM, Bushong EA, Ramachandra R, Peltier ST, Ellisman MH.
865 High-performance serial block-face SEM of nonconductive biological samples enabled by
866 focal gas injection-based charge compensation. J Microsc. 2018;270(2):142-9. Epub
867 2017/12/02. doi: 10.1111/jmi.12667. PubMed PMID: 29194648; PubMed Central PMCID:
868 PMCPMC5910240.

869 71. Schindelin J, Arganda-Carreras I, Frise E, Kaynig V, Longair M, Pietzsch T, et al.
870 Fiji: an open-source platform for biological-image analysis. Nat Methods. 2012;9(7):676-82.
871 Epub 2012/06/30. doi: 10.1038/nmeth.2019. PubMed PMID: 22743772; PubMed Central
872 PMCID: PMCPMC3855844.

873 72. Arganda-Carreras I, Sorzano COS, Marabini R, Carazo JM, Ortiz-de Solorzano C,
874 Kybic J. Elastic Registration of Histological Sections using Vector-Spline Regularization. In:
875 Beichel RD, Sonka M, editors. Computer Vision Approaches to Medical Image Analysis.
876 Berlin, Heidelberg: Springer; 2006. p. 85-95.

877 73. Cardona A, Saalfeld S, Schindelin J, Arganda-Carreras I, Preibisch S, Longair M, et
878 al. TrakEM2 software for neural circuit reconstruction. PLoS One. 2012;7(6):e38011. Epub
879 2012/06/23. doi: 10.1371/journal.pone.0038011. PubMed PMID: 22723842; PubMed Central
880 PMCID: PMCPMC3378562.

881 74. Bolte S, Cordelieres FP. A guided tour into subcellular colocalization analysis in light
882 microscopy. J Microsc. 2006;224(Pt 3):213-32. Epub 2007/01/11. doi: 10.1111/j.1365-
883 2818.2006.01706.x. PubMed PMID: 17210054.

884 75. Bates D, Mächler M, Bolker B, Walker S. Fitting Linear Mixed-Effects Models Using
885 lme4. Journal of Statistical Software. 2015;67:1-48. doi: 10.18637/jss.v067.i01.

886 76. Fox J, Weisberg S. An R Companion to Applied Regression. Third ed. Thousand Oaks
887 CA: Sage; 2019.

888 77. Searle SR, Speed FM, Milliken GA. Population Marginal Means in the Linear Model:
889 An Alternative to Least Squares Means. The American Statistician. 1980;34(4):216-21. doi:
890 10.1080/00031305.1980.10483031.
891

892

Supporting Figure Legends

Figure S1. HFD and genetic lipid overflow models do not disrupt growth and developmental timing.
(**A-C**) Graphs compare STD and HFD animals, indicating that they have similar larval weight (mg), nephrocyte volume (μm^3) and developmental timing (% pupariation versus hours after larval hatching).
(**D-F**) Graphs compare STD animals expressing ATGL in the fat body (*Lpp>ATGL*) with controls (*Lpp-GAL4*). indicating that they have similar larval weight (mg), nephrocyte volume (μm^3) and developmental timing (% pupariation versus hours after larval hatching). Note that nephrocyte size is significantly different ($p<0.0005$) between control and ATGL expressing animals.

Figure S2. Time course of dextran uptake in nephrocytes.
(**A-B**) Graphs quantify individual uptake (A) and uptake ratio (B) of fluorescently labelled 500 kDa and 10 kDa dextrans as a function of time (min) for *ex vivo* pericardial nephrocytes.

Figure S3. CLEM analysis of endolysosomes in STD nephrocytes.
(**A**) The five endolysosomal categories distinguished in correlative light-electron microscopy (CLEM) analysis of *Rab7::YFP^{myc}* STD nephrocytes subjected to dextran uptake assays. The criteria used were scanning EM luminal density ("white", "light" or "dark"), and also the "+" or "-" status of expression of Dextran and Rab7::GFP. Scale bar = 1 µm.
(**B**) Quantitations from SBF SEM volumes of a STD control and a STD *Rab7::YFP^{myc}* nephrocyte showing similar endosome size distributions. Note that "white" and "light" endosomes but not "dark" endolysosomes were segmented and quantified per cell according to their diameter (µm).

Figure S4. DGAT1 knockdown increases nephrocyte lipid peroxidation.
(**A**) Confocal panels represent ratio of oxidized (500-540 nm emission) to non-oxidized (570-610 nm emission) forms of the lipid peroxidation sensor BODIPY 581/591 C11 in pericardial nephrocytes (dotted outlines) from STD larvae and HFD larvae carrying *Dot>DGAT1[i]* or *Dot>ATGL*.
(**B**) Graph quantifies oxidized: non-oxidized ratios of the lipid peroxidation sensor BODIPY 581/591 C11 in pericardial nephrocytes for the dietary and genetic manipulations in A. On HFD, lipid peroxidation is increased by *DGAT1* knockdown but not by *ATGL* expression.

Figure S5. *Srl* knockdown prevents ATGL rescue of dextran uptake.
(**A**) *Delg* or *Srl* knockdown decreases mitochondrial volume in STD nephrocytes. Quantitation of mitochondrial volumes (as % of cell volume) of STD pericardial nephrocytes for control (*Dot>*), *Dot>Delg[i]* and *Dot> Srl[i]* larvae.
(**B**) Confocal panels show 10 kDa and 500 kDa dextran uptake in *ex vivo* pericardial nephrocytes of control (*Dot>*) and *Dot>ATGL; Srl[i]* larvae on HFD. The dextran signals of both genotypes, imaged within the same field of view, are comparable. Graph shows small but significant *decrease* in 10 kDa and 500 kDa dextran uptake between control (*Dot>*) and *Dot>ATGL; Srl[i]* larvae on HFD. Note that in the absence of Srl knockdown, ATGL significantly *increases* dextran uptake on HFD.

Movie S1. SBF SEM Z stack of a STD nephrocyte. Data were collected with a 0.1 µm step size and recorded at 25 fps.

Movie S2. SBF SEM Z stack of a HFD nephrocyte. Data were collected with a 0.1 µm step size and recorded at 25 fps.

Movie S3. SBF SEM Z stack of a *Dot>DGAT1[i]* HFD nephrocyte. Data were collected with a 0.1 µm step size and recorded at 25 fps.

Movie S4. SBF SEM Z stack of a *Dot>ATGL* HFD nephrocyte. Data were collected with a 0.1 µm step size and recorded at 25 fps.

Table S1. Summary of statistical methods and analysis. For each main and supporting figure, the linear mixed models, statistical inference tests and p values are shown.

Figure 1

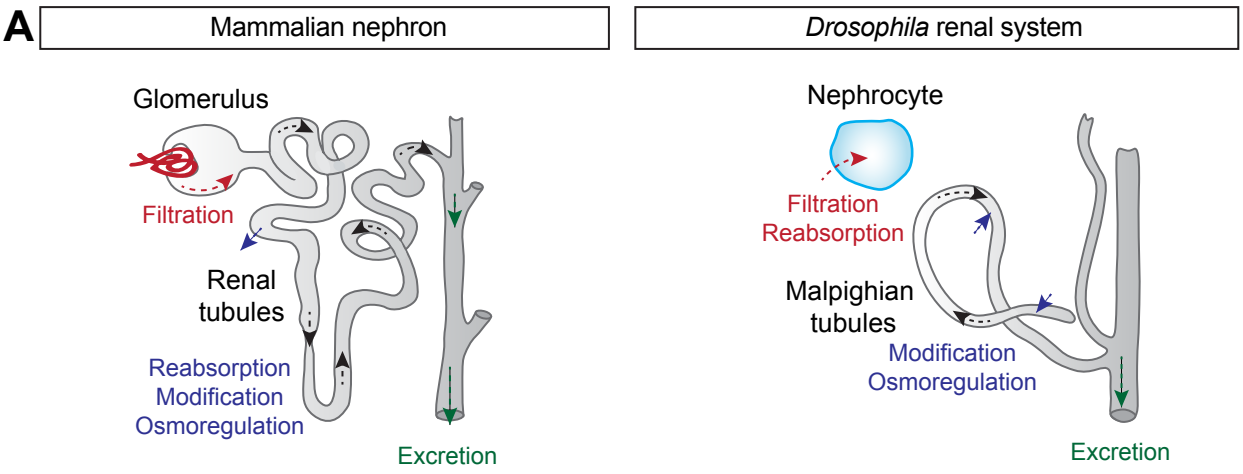

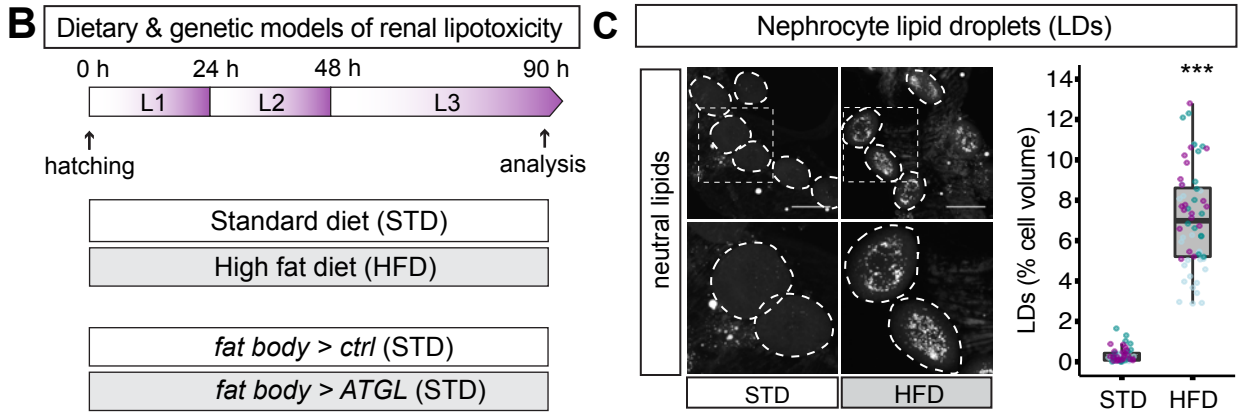

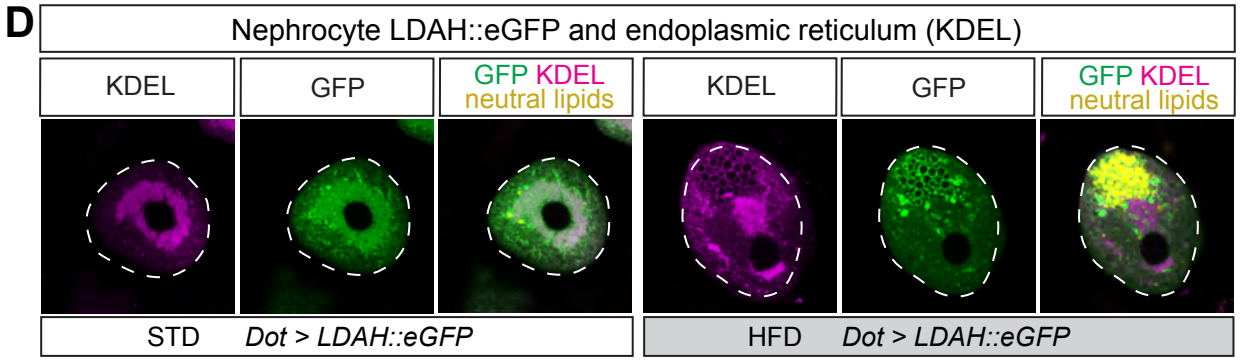

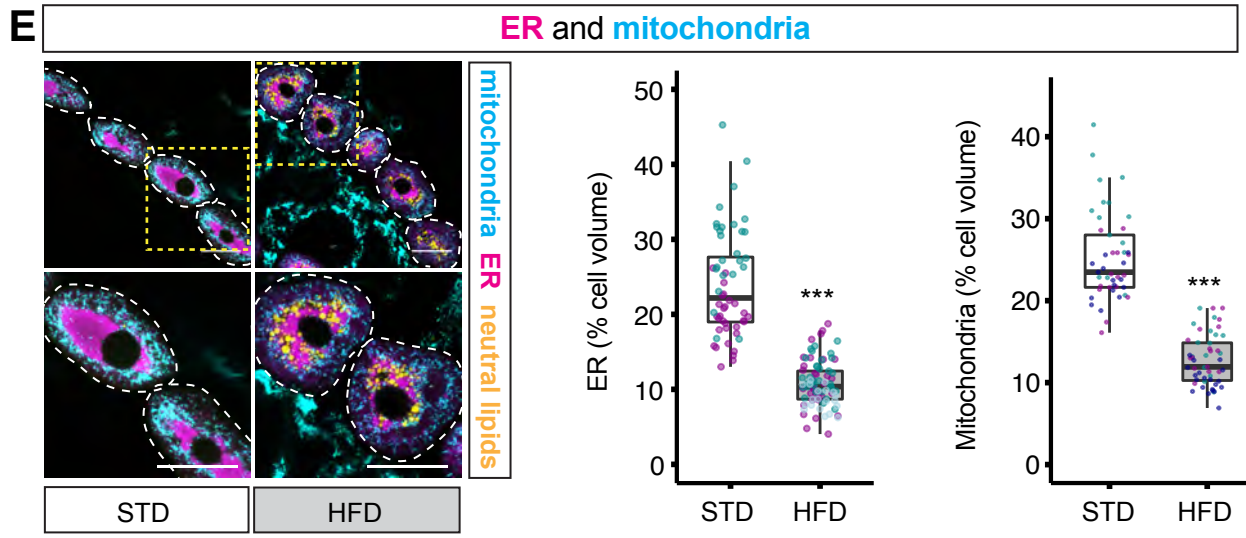

Figure 2

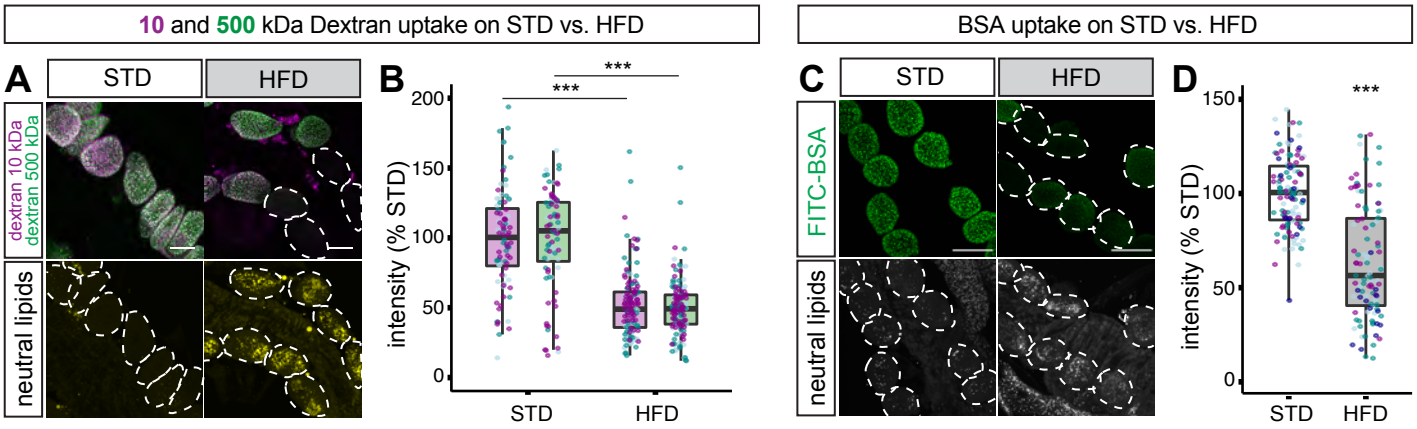

Figure 3

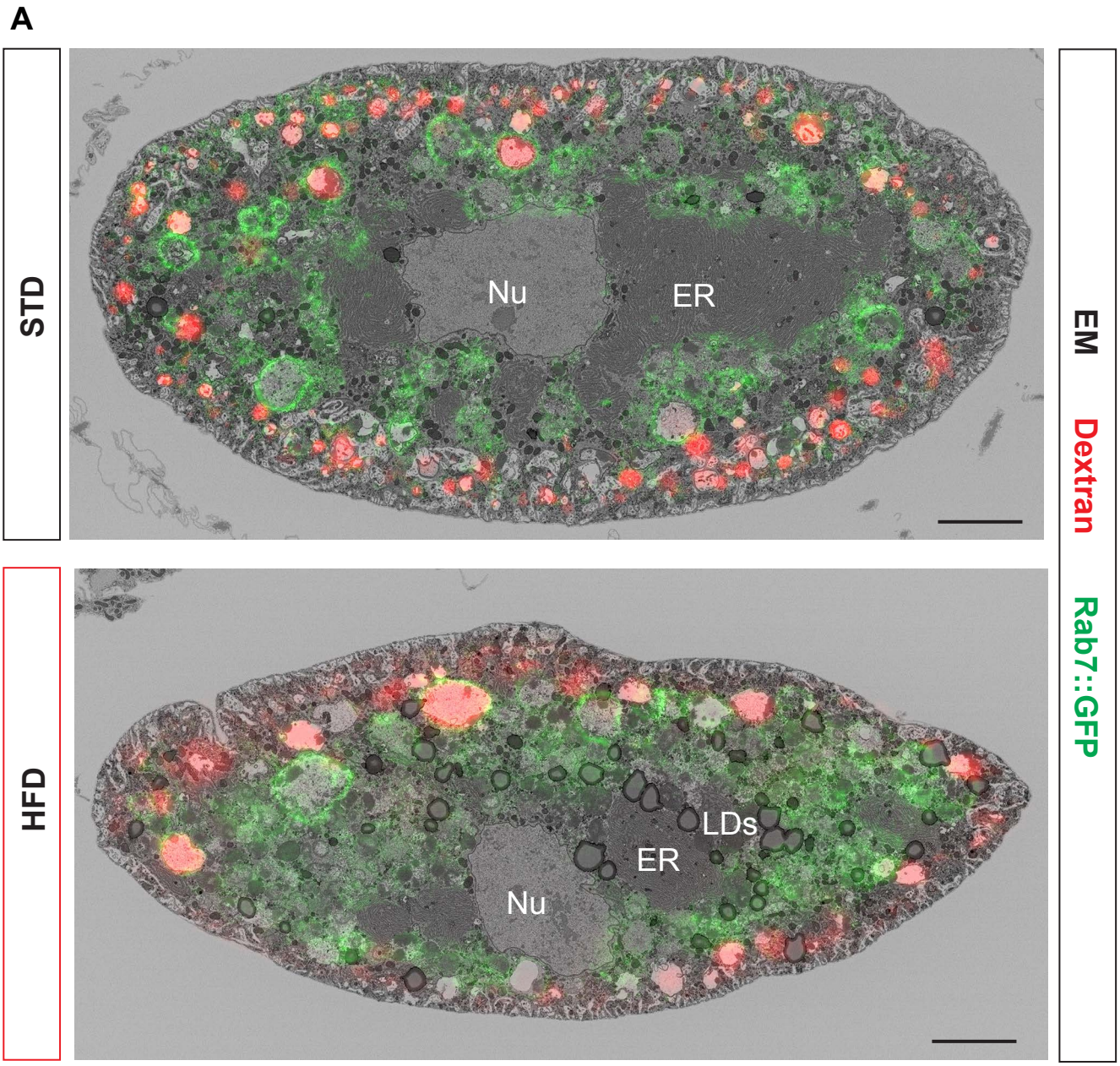

Figure 4

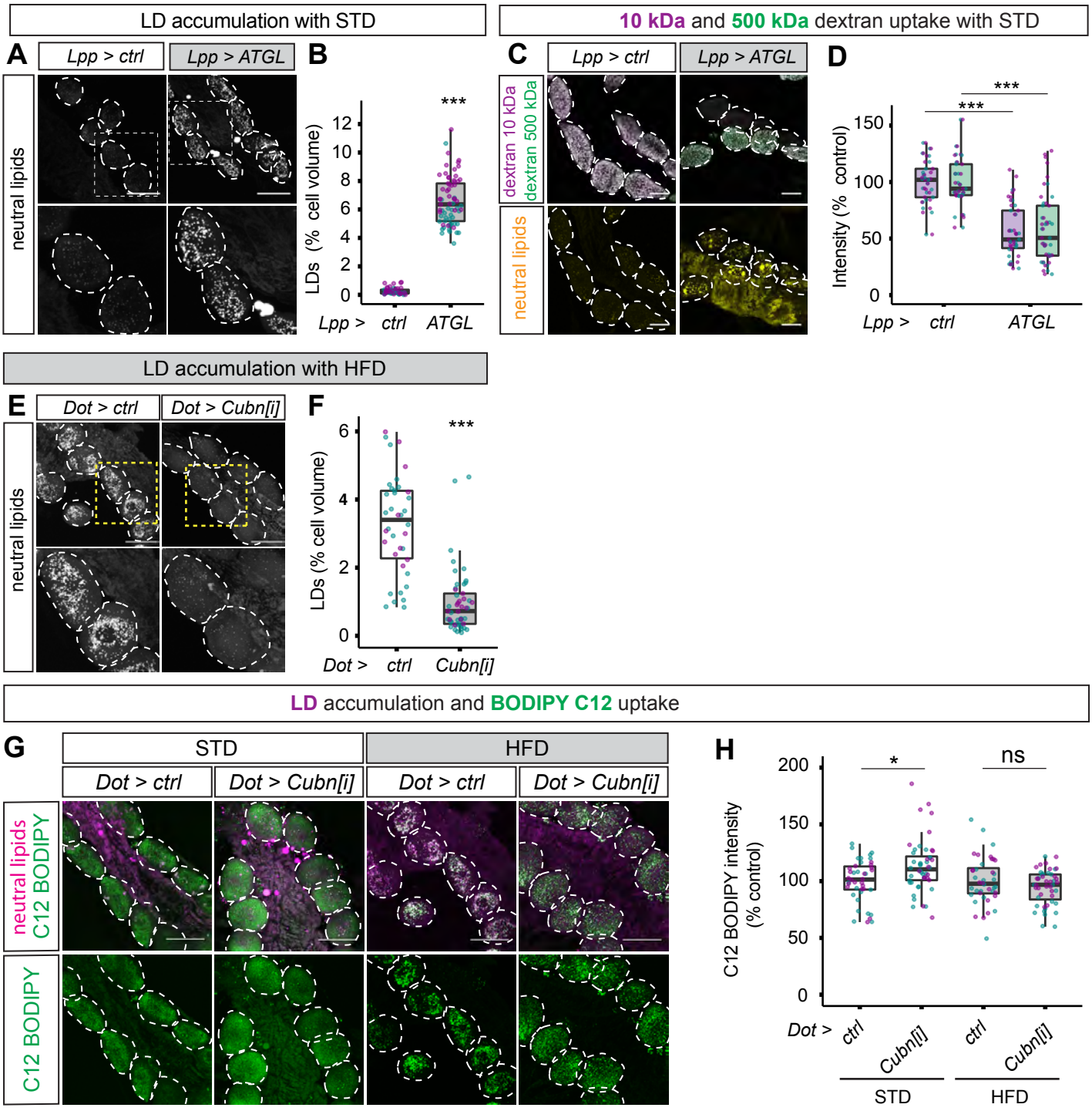

Figure 5

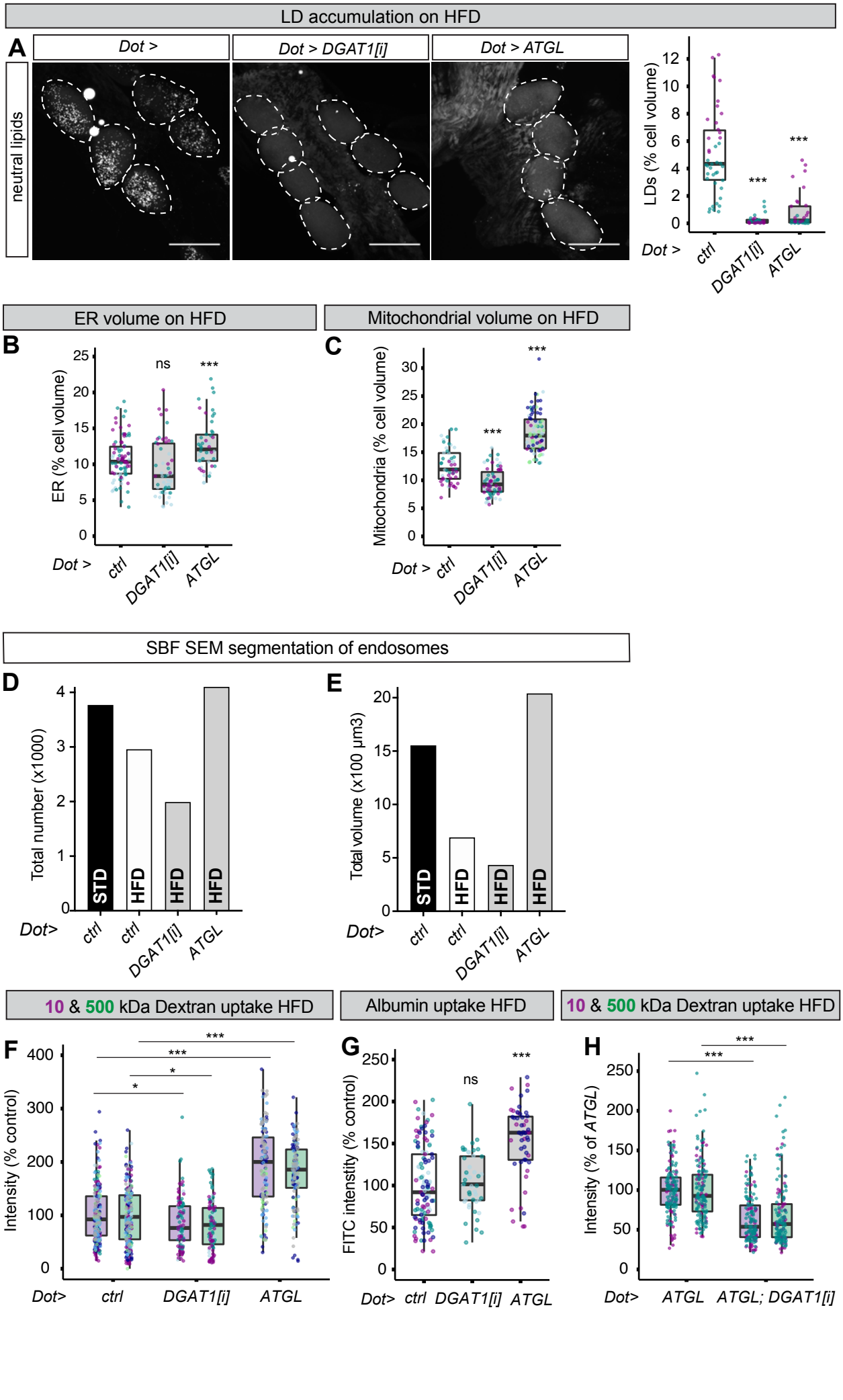

Figure 6

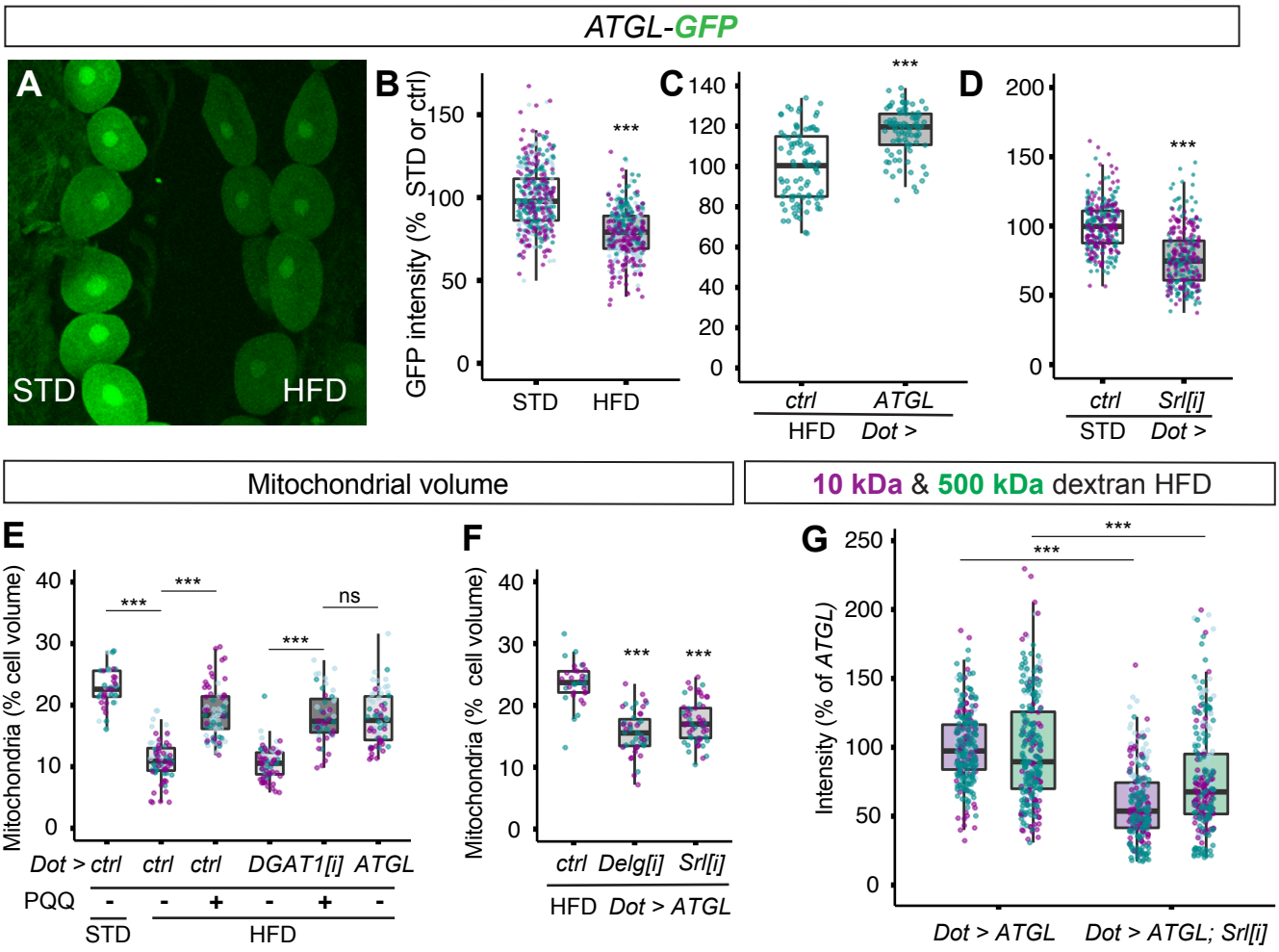

Figure S1

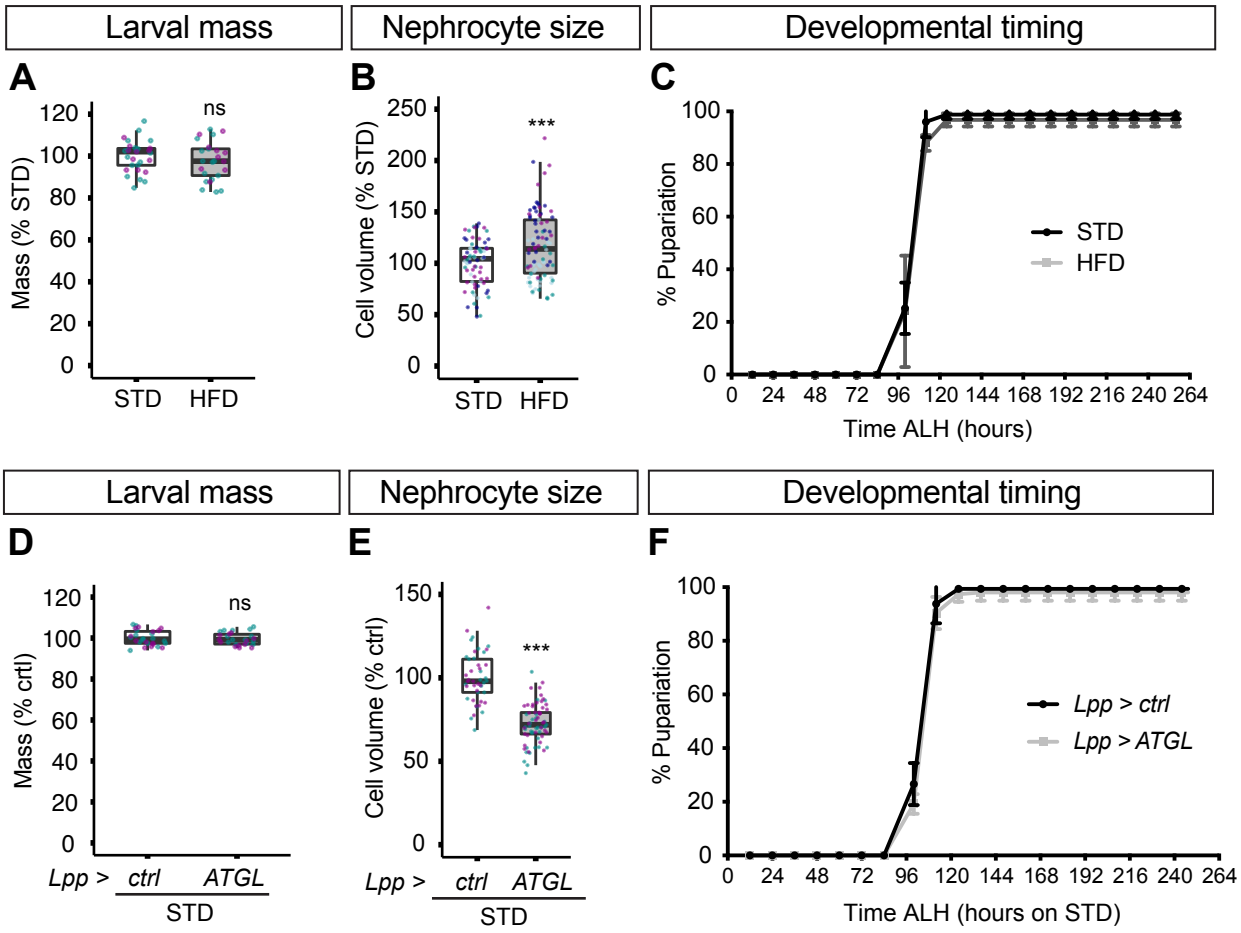

Figure S2

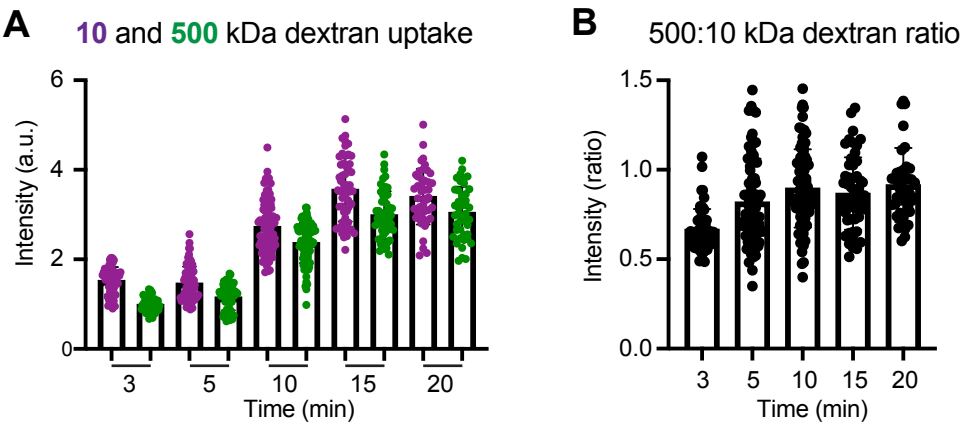

Figure S3

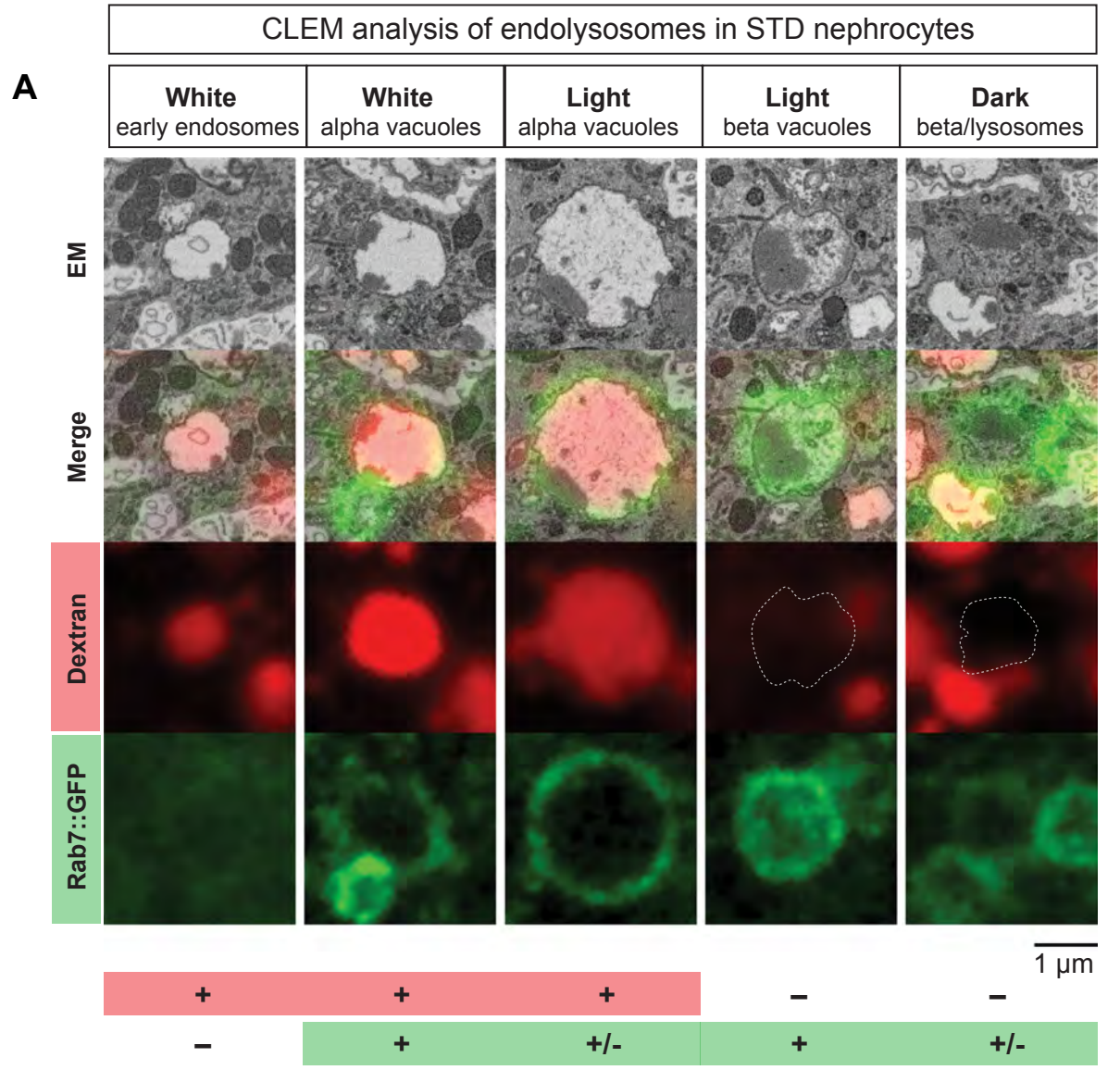

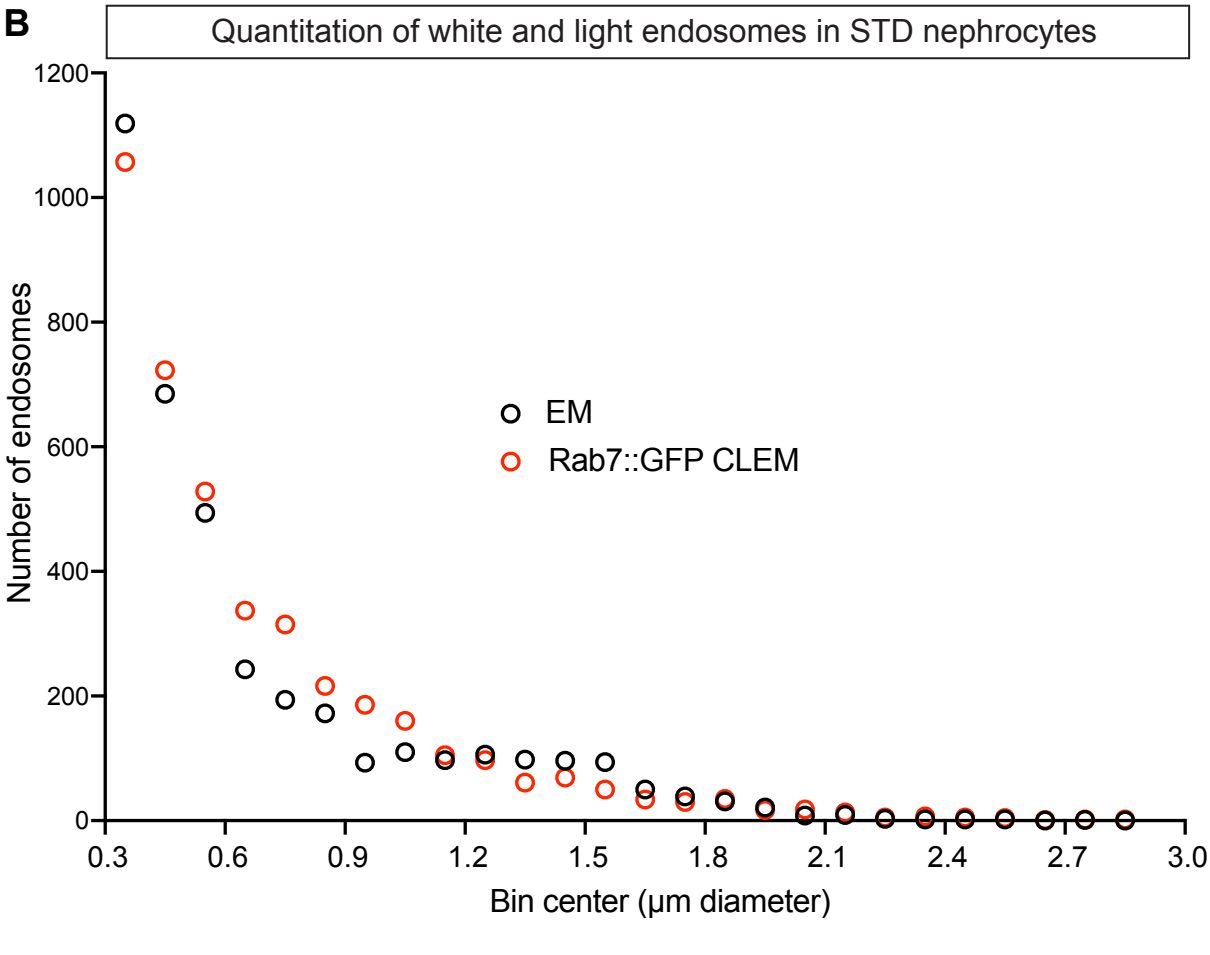

Figure S4

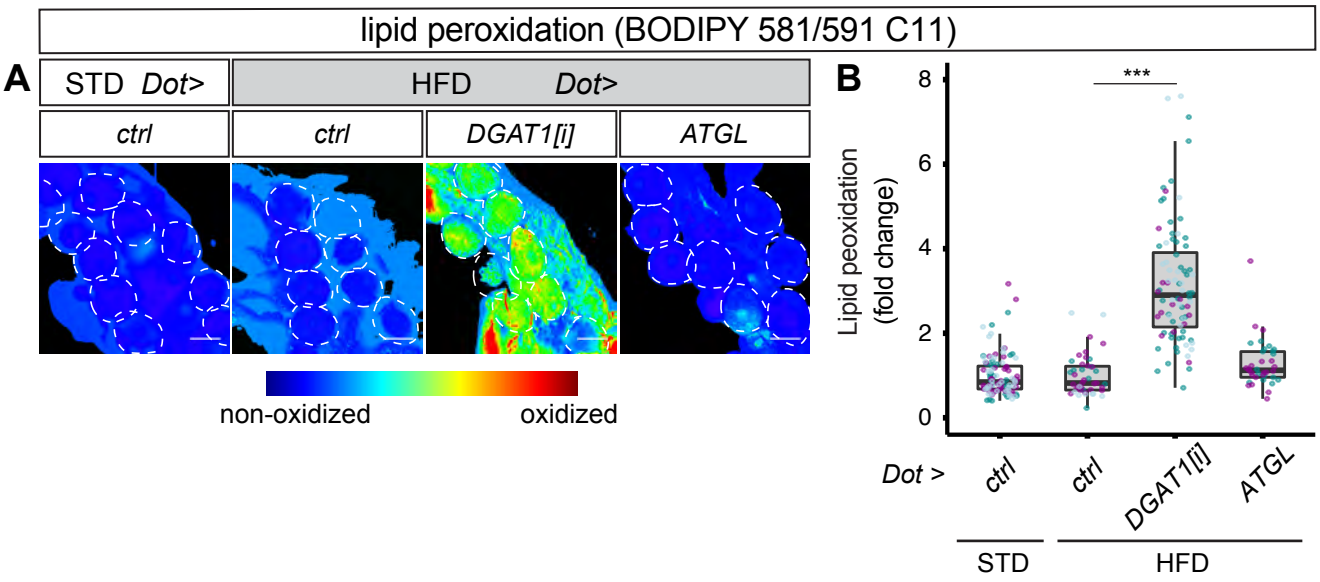

Figure S5